SiGe nanostructures: new insights into growth processes

SiGe nanostructures: new insights into growth processes

I Berbezier[1], A Ronda[1] and A Portavoce[1,2]

[1] CRMC2-CNRS Campus de Luminy, Case 913, F13288 Marseille Cedex 9, France
[2] L2MP-CNRS, Av. Escandrille Normandie-Niemen, Case 151, F13397 Marseille Cedex 13, France

E-mail: berbezier@crmc2.univ-mrs.fr

Abstract
During the last decade, $Si/Si_{1-x}Ge_x$ heterostructures have emerged as a viable
system for use in CMOS technology with the recent industrial production of
heterojunction bipolar transistor-based integrated circuits. However, many key
problems have to be solved to further expand the capabilities of this system
to other more attractive devices. This paper gives a comprehensive review of
the progress achieved during the last few years in the understanding of some
fundamental growth mechanisms. The discrepancies between classical theories
(in the framework of continuum elasticity) and experimental results are also
specially addressed. In particular, the major role played by kinetics in the
morphological evolution of layers is particularly emphasized. Starting from the
unexpected differences in $Si_{1-x}Ge_x$ morphological evolution when deposited
on (001) and on (111), our review then focuses on: (1) the strain control and
adjustment (from fully strained to fully relaxed 2D and 3D nanostructures)—
in particular, some original examples of local CBED stress measurements
are presented; (2) the nucleation, growth, and self-assembly processes, using
self-patterned template layers and surfactant-mediated growth; (3) the doping
processes (using B for type p and Sb for type n) and the limitations induced
by dopant redistribution during and after growth due to diffusion, segregation,
and desorption. The final section will briefly address some relevant optical
properties of $Si_{1-x}Ge_x$ strained layers using special growth processes.

(Some figures in this article are in colour only in the electronic version)

1. Introduction

Let us first consider the impact of $Si_{1-x}Ge_x$ heterojunctions on the CMOS production line
and the future prospects of this technology. The first $Si_{1-x}Ge_x$-based device to have been
integrated with a conventional CMOS production line is the heterojunction bipolar transistor

(HBT). The main reason is that it presents a minimum additional cost to CMOS and a very simple design with a narrow $Si_{1-x}Ge_x$ base layer inserted into a bipolar BiCMOS fabrication process. However, even if this technology is quite mature, the device characteristics obtained in production lines are much less good than those demonstrated for research devices. This result has not been explained so far, but the high thermal budget, used in present CMOS production, is assumed to have the major detrimental effect. Indeed, it causes strain relaxation (by dislocation nucleation and also by interdiffusion of $Si/Si_{1-x}Ge_x$), dopant diffusion, interface roughening, and Ge clustering. All these phenomena are well known to degrade the electrical properties of HBTs.

Recent research developments also focus on other attractive devices such as the p-type $Si_{1-x}Ge_x$ MOSFET, since p channels represent so far the major limiting factor in CMOS performance. Indeed, the mobility of $Si_{1-x}Ge_x$ p MOSFET is only 20% larger than those of conventional transistors. This is attributed to parallel conduction due to the small band offset of $Si_{1-x}Ge_x$ channels that contain low Ge content. Further improvements would then rely on an increase of the Ge content to increase the band offset. This is expected to give stronger transfer and confinement of the carriers, preventing parallel conduction from taking place. However, this faces serious problems, since at large Ge contents, both the critical thickness of dislocation nucleation (h_{cr}) and the critical thickness of 2D–3D growth transition (H_{SK}) are very low. A good control and understanding of stress relaxation in 2D wells is consequently a major issue to address for these devices.

Recently, the most striking performances have been reported for $Si_{1-x}Ge_x$ modulation-doped field effect transistors (MODFETs) grown on virtual substrates (fully relaxed by a network of misfit dislocations (MDs)) yielding faster transistors than any other p-channel transistor in the literature [1]. In spite of the high mobility achieved, the overall success of $Si_{1-x}Ge_x$ MODFETs has so far been limited because of the high dislocation density and the poor surface morphology (cross-hatch pattern) which impair further the processing of the structures. Since the cross-hatch pattern originates from the MDs lying mainly in the graded buffer layer, the search for new processes of fabrication of the relaxed buffer layer is a hot topic.

Finally for the future, alternative routes to CMOS technology should also be developed for feature sizes approaching 50–30 nm. A new generation of nanometric devices should then be found as a matter of urgency, in order to permit the current scaling trend to continue, following the conventional CMOS approach. For this reason, many new quantum device concepts have recently been reported in the literature. However, there are major bottlenecks in the development of these emerging devices relating to:

 (1) the morphology, composition, and self-assembly of 1D and 0D nanostructures (e.g. for nanocrystal memory);
 (2) the control and reduction of spatial distribution of dopants in highly doped quantum wells (e.g. for resonant tunnelling diodes);
 (3) the realization of virtual substrates (e.g. for laser cascade).

As a consequence, for the majority of present or future devices, the improvement of the device features mainly depends on a better understanding (and control) of the fundamental processes of growth (strain control and adjustment, composition and morphology, and dopant incorporation).

The paper is organized as follows. Section 2 will briefly recall the techniques and the experimental conditions used for the growth and characterization (composition, microstructure, morphology, and physical properties) of $Si_{1-x}Ge_x$ nanostructures.

Section 3 is devoted to the strain adjustment and control. First, the elastic energy and the critical thickness of dislocation nucleation calculated for two nominal orientations Si(001) and (111) will be compared to the experimental results obtained. Then the local measurement of stress in highly strained structures (2D and 3D) will be reported. Deviations from the standard elastic theories due to kinetics and to Si/Ge interdiffusion processes will be evidenced. At the end, the microstructure and morphology of relaxed $Si_{1-x}Ge_x$ channels on top of virtual substrates (relaxed $Si_{1-x}Ge_x$ buffers) will be discussed. Some key processes used to pin the propagation of dislocations towards the top layer will be presented.

In section 4, kinetic and stress-driven instabilities, growth, and self-assembly processes will be reviewed. Kinetic phase diagrams of $Si_{1-x}Ge_x$ morphologies with the deposited thickness and the stress (Ge concentration) have been drawn. The morphological evolution of $Si_{1-x}Ge_x$ layers deposited on Si(001) and (111) are compared. The influence of step density, substrate orientation, miscut angle, and kinetics on the instability will be analysed. A comparison between kinetic and stress-driven instability will also be presented. At the end, the improvement provided by either a two-step process or by surfactant-mediated growth will be evidenced.

Section 5 will show new insights into dopant redistribution processes (during and after growth). In particular, the separate effects of stress and composition on bulk diffusion, kinetic segregation, and desorption will be introduced. Different processes of dopant incorporation are compared. We finally discuss further the segregation effect of p-type (B) and n-type (Sb) dopants.

In the remainder of the paper we will briefly review some relevant PL characterizations of nanostructures grown by solid-source or gas-source molecular beam epitaxy (MBE).

2. Experimental details

Most of the $Si_{1-x}Ge_x$ nanostructures were grown using RIBER solid-source molecular beam epitaxy (SSMBE) equipment with a background pressure in the 10^{-11} Torr range [2]. Si and Ge were evaporated from an electron gun evaporator and an effusion cell, respectively, with beam fluxes calibrated *in situ* by reflection high-energy electron diffraction (RHEED) oscillations and *ex situ* by x-ray diffraction (XRD) to provide accurate control of the alloy ratio. For both Si and Ge, the fluxes used resulted in a growth rate of about 1 nm min^{-1}. Sb and B were evaporated from effusion cells with fluxes calibrated *ex situ* by secondary-ion mass spectrometry (SIMS). At low temperatures, the substrate temperature was calibrated using the melting point of In and Ga and extrapolated with a power law, and in the high-temperature (HT) range ($T > 500\,°C$) it was measured with an optical pyrometer. Growth temperatures ranged between 350 and 750 °C.

For comparison, some $Si_{1-x}Ge_x$ layers were also grown using a modified VG Semicon gas-source molecular beam epitaxy (GSMBE) cold-wall system with a 2×10^{-11} Torr background pressure [3]. Disilane (Si_2H_6) and germane (GeH_4) were used as Si and Ge sources respectively and diborane (B_2H_6 diluted to 1% by argon) as the source of boron doping. During continuous doping experiments, B/Si flux ratios (B_2H_6/Si_2H_6) were varied between 4×10^{-4} and 6×10^{-3}. For experiments involving the pre-adsorption of B, the flux of Si_2H_6 was turned off and B_2H_6 was adsorbed on the Si(001) buffer layer at temperatures between 450 and 650 °C.

Prior to loading in the growth chamber, samples were chemically cleaned using the Shiraki process, which leaves the surface covered by a protective oxide layer. *In situ* cleaning consisted of a two temperature process (850 °C/30 min + 1230 °C/2 min), which removes the oxide layer by sublimation, and results in a sharp 2D RHEED pattern indicative of a defect-free surface. 7×7 and 2×1 surface reconstructions were observed on Si(111) and (001), respectively.

Prior to the growth of $Si_{1-x}Ge_x$ layers, a 20 nm thick Si buffer layer was systematically grown at 750 °C in order to obtain a reproducible surface. Si wafers of microelectronic grade were used with misorientations varying between 0° and 10° (with an angle precision of 0.5°). The misorientations were systematically checked by means of Laue diffraction.

Transmission electron microscopy (TEM) investigations were performed using a Jeol 2000FX equipped with an energy dispersive spectrometer (EDS) for x-ray analysis. High-spatial-resolution quantitative analyses were performed by means of convergent beam electron diffraction (CBED) and EDS in a field effect analytical microscope (Jeol 2010 FEG) with high-convergence coils. Diffraction patterns were recorded at 200 kV with a typical convergence half-angle of 20 mrad and a minimum 2.4 nm probe size. Lattice imaging was achieved using a Jeol 4000EX microscope operating at 400 kV with a point-to-point resolution of 0.14 nm. Both plan- and cross-section-view geometries have been investigated in order to cross-check relaxation measurements. Cross-section TEM samples were prepared by mechanical polishing down to 20 μm and subsequent Ar-ion milling to perforation. Plan-view samples were prepared by chemical etching. Moreover, CBED experiments have been repeated on several samples, in various geometries, but also along various axes, to avoid artefacts and accidental relaxation during the preparation of TEM thin samples.

Grazing incidence x-ray diffraction (GIXRD) experiments were performed using a high-resolution triple-axis diffractometer coupled with a rotating anode x-ray generator. X-ray scattering measurements were recorded with a beam wavelength of 0.154 nm. Investigations focused on the (220), (004), and (111) bulk diffraction peaks. The statistical description of the surface was obtained thanks to reflectivity measurements that probe the surface as regards the long-range order (for details see [4]).

Morphological characterization was performed by atomic force microscopy (AFM) in air in non-contact mode. To analyse the formation of 3D patterns we mainly investigated two parameters: the root mean square (rms) roughness on 5×5 μm^2 areas and the self-correlation function (to measure the periodicity of the pattern).

The dopant concentration profiles (B and Sb) were measured from SIMS using a Cameca IMS4F operated at 12.5 keV with O^{2+} primary ions.

For the segregation/diffusion studies the samples were grown using a specific cycle of growth that enables us to determine both segregation and diffusion coefficients for every sample.

Moreover, double sequences of $(Ge/Si_{1-x}Ge_x)$ structures separated by a Si cap layer sufficiently thick (about 20 nm) to avoid coupling effects between the active wells were also elaborated in order to allow both AFM and photoluminescence (PL) characterization on the same sample.

PL was excited by the 514 nm line of an Ar^+ laser with power densities between 6 and 200 mW mm^{-2} and was detected by a nitrogen-cooled Ge detector in a lock-in configuration [5].

All the results presented hereafter are extracted from a compilation of several experiments performed on a large number of samples with a large range of Ge concentrations. They are reproducible under our growth conditions.

3. Strain adjustment and control

3.1. Highly strained structures

Before presenting the experimental results on the stress-relief mechanisms in $Si_{1-x}Ge_x(111)$ and (001) [6, 7] let us consider the predictions that can be deduced from the calculation of elastic energy at different misfits.
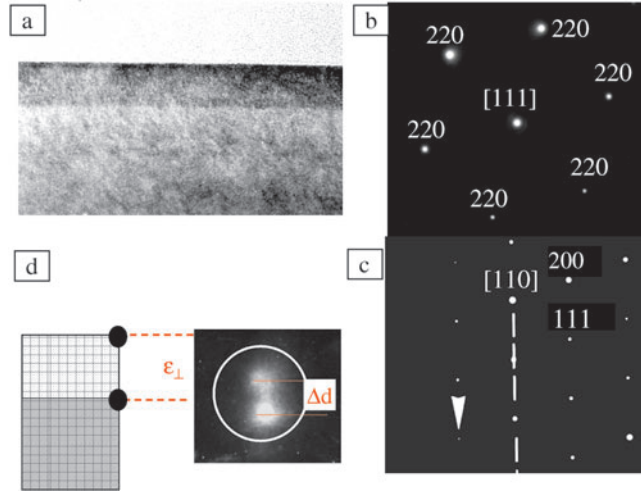
Figure 1. (a) A TEM cross-section view of the ~20 nm thick $Si_{0.85}Ge_{0.15}$ deposited on Si(111). TED patterns with (b) [111] and (c) [110] zone axes. (d) A schematic view of the tetragonal distortion.

At low misfits, the thin planar epitaxial layer is expected to be coherent with the thick Si substrate. The strain of the epilayer lattice is described by the standard linear elasticity theory (Hooke's law):

$$\sigma_{ij} = [\mathbf{C}]\varepsilon_{kl} \qquad (1)$$

where σ_{ij} and ε_{kl} are the stress and strain tensors, respectively, and $[\mathbf{C}]$ is the elastic constants matrix.

For the growth of $Si_{1-x}Ge_x$ on Si(100), the film is biaxially compressed in the growth plane and expands in the direction perpendicular to it. Therefore, $\varepsilon_1 = \varepsilon_2 = -m$ where m is the misfit defined by $(a_{SiGe} - a_{Si})/a_{Si}$ with a_{SiGe} and a_{Si} the $Si_{1-x}Ge_x$ and Si lattice parameters respectively. ε_3 is the tetragonal distortion of the layer ($\varepsilon_\perp$). For the growth on Si(001), $\varepsilon_\perp$ is described by

$$\varepsilon_\perp = (-2\nu)m/(1-\nu) = -2mC_{12}/C_{11} \qquad (2)$$

where ν is Poisson's ratio and C_{ij} are the appropriate elastic constants of the $Si_{1-x}Ge_x$ alloy.

For the growth on (111), the film is anisotropically compressed along the $\langle 110 \rangle$ and $\langle 112 \rangle$; the elastic and shear moduli and the Poisson's ratio must be decomposed along these two directions. The tetragonal distortion is then described by

$$\varepsilon_\perp = 2m[C_{11} + 2C_{12} - 2C_{44}]/[C_{11} + 2C_{12} + 4C_{44}]. \qquad (3)$$

The elastic energy stored inside the layer (E_{el}) is given by

$$E_{el} = 2\mu m^2(1+\nu)/(1-\nu) \text{ (GPa)}. \qquad (4)$$

It is important to remark here, regarding the expressions given above, that a larger tetragonal distortion and a lower elastic energy are expected on Si(001) than on Si(111). Table 1 gives the calculated values of $\varepsilon_\perp$ for two concentrations of Ge.

In a preliminary experiment, $\varepsilon_\perp$ can be simply detected from transmission electron diffraction (TED) patterns as shown in figure 1 for a ~20 nm thick $Si_{1-x}Ge_x$ layer deposited on Si(111) with $x = 0.15$ ($m = 0.63\%$). In this case, the cell is fully coherent with the substrate; consequently only one series of diffraction spots are observed on the plan-view pattern ([111]
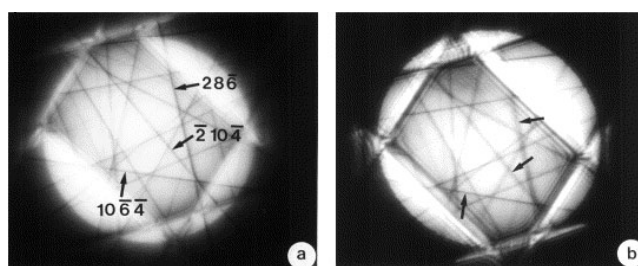
Figure 2. CBED patterns recorded in the plan-view geometry along the [4 3 5] axis for (a) the single (111) Si substrate and (b) the superimposition of the substrate and the 20 nm thick, flat, tetragonally distorted $Si_{0.85}Ge_{0.15}$ layer. The $(10\ \bar{6}\ \bar{4})$ HOLZ line, corresponding to a plane perpendicular to the surface, is not split, testifying a fully strained in-plane lattice parameter. The $(2\ 8\ \bar{6})$ and $(\bar{2}\ 10\ \bar{4})$ lines, corresponding to planes parallel to the surface, are split, giving rise to a normal lattice parameter misfit.

Table 1. Tetragonal distortion calculated from the elasticity theory.

Ge content (%)	$x = 0.15$	$x = 0.30$
Misfit	0.63	1.2
$\varepsilon_\perp^{(111)}$	0.27	0.5
$\varepsilon_\perp^{(001)}$	0.46	0.9

zone axis; figure 1(b)), while two series of spots aligned along the growth direction are observed in the cross-section pattern ([110] zone axis; figure 1(c)). However, because of the limited resolution of this technique, it is not possible to accurately measure the tetragonal distortion (in this case, the Δd expected is $\sim 8 \times 10^{-4}$ nm).

Complementary and more accurate information can be deduced from CBED as shown in figure 2 [6, 7]. Experiments were performed on a thick area (thicker than 100 nm) of a plan-view sample in order to minimize the relaxation in the substrate. The sample was tilted from the [111] axis along a ⟨220⟩ Kikuchi band. Figure 2 displays [3–5] CBED patterns recorded on (a) the bare substrate and (b) the superimposed substrate/epilayer system.

The tetragonal distortion can be observed as a splitting of Bragg contours relative to crystallographic planes inclined at an angle with respect to the substrate plane. The tetragonal distortion ($\varepsilon_\perp$) may then be deduced from the relative rotation (θ_r) of the planes via [8]

$$\Delta\theta_r = \varepsilon_\perp (\sin 2\theta)/2.$$

From the measurement of the splitting of the $(2\ 8\ \bar{6})$ and $(\bar{2}\ 10\ \bar{4})$ lines, we deduced a value of $\varepsilon_\perp = 2.4 \times 10^{-3}$, corresponding to a misfit $m = 6 \times 10^{-3}$, and Ge concentration $x = 0.14$, in good agreement with the nominal concentration of the layer investigated. It should be noted that the HOLZ line of the plane, perpendicular to the surface, is not split. This confirms the presence of a purely tetragonal distortion.

We would like to stress that similar morphology (flat surface, uniformity and free of dislocation) occurred also with (001) layers in this low range of strain and thus will not be shown here.

In order to determine the local distribution inside an undulating layer, the technique was next applied to nanometre scale areas at the crest of a $Si_{0.7}Ge_{0.3}(001)$ undulation: along a cross-section line and in plan-view geometry [6, 7]. As an example, one set of experiments (cross-section view) recorded along the [15 $\bar{7}$ 0] axis are discussed hereafter. Other views along other axes lead to the same conclusions. The cross-sectional sample was tilted from the [0 0 1] axis along a ⟨220⟩ Kikuchi band. A series of CBED patterns recorded along
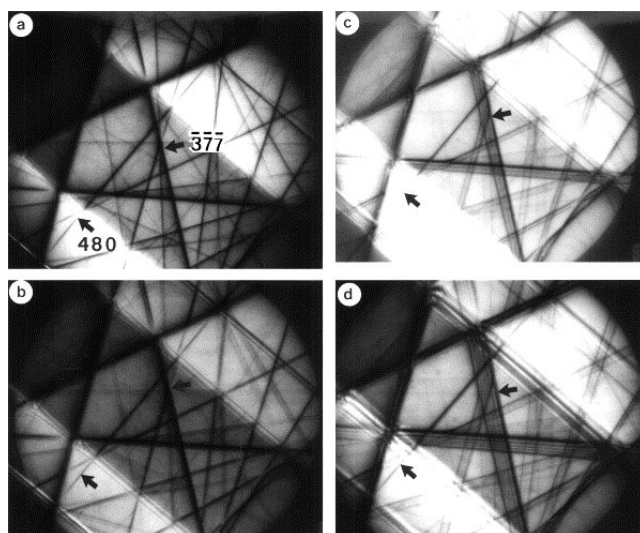
Figure 3. Evolution of the CBED patterns recorded along the [15 $\bar{7}$ 0] axis, in cross-section geometry, on an undulating (100) $Si_{0.7}Ge_{0.3}$ layer. The nanoscale electron beam was focused along a line starting from (a) the (100) Si substrate, (b)–(d) towards the topmost free surface of an undulation. The (480) HOLZ line, corresponding to a plane perpendicular to the (001) surface, does not display any noticeable splitting, leading to a fully strained in-plane lattice parameter. The ($\bar{3}\,\bar{7}\,\bar{7}$) HOLZ line, corresponding to a plane parallel to the surface, shows a gradual splitting, from the substrate towards the crest of the undulation, testifying to a gradual relaxation in the direction normal to the surface.

the [15 $\bar{7}$ 0] axis is presented in figure 3. The Si substrate reference pattern is displayed in figure 3(a). Figures 3(b)–(d) show the gradual increase of the ($3\,\bar{7}\,\bar{7}$) HOLZ lines splitting when the electron beam is displaced in the direction of the topmost $Si_{0.7}Ge_{0.3}$ surface. This is indicative of a gradual relaxation along the z-axis. It should be pointed out that the splitting of the (4 8 0) HOLZ line corresponding to a plane perpendicular to (001) is negligible. This is representative of a $Si_{0.7}Ge_{0.3}$ cell fully strained in the (001) plane. Regarding the plan-view geometry (patterns recorded along [1 1 11]) we observed that the splitting of the (9 3 $\bar{1}$) and (3 9 $\bar{1}$) HOLZ lines, corresponding to planes symmetrical about the [0 0 1] axis were not equal. This was attributed to a triclinic deformation of the $Si_{0.7}Ge_{0.3}$ cell which was explained by the tetragonal distortion at the top of the undulation being larger than that at the bottom [7].

In order to obtain a more comprehensive analysis of the strain fields in the undulated $Si_{0.7}Ge_{0.3}(001)$ layer, we also performed GIXRD studies [7]. The scans parallel and perpendicular to the surface confirmed:

 (i) the tetragonal distortion of the (004) planes parallel to the surface, in good agreement with the value of $\varepsilon_\perp$ predicted for $x = 0.3$ [7]; and

 (ii) the perfect fit between Si and $Si_{0.7}Ge_{0.3}(220)$ planes perpendicular to the surface proving the absence of elastic relaxation (figure 4(b)).

This confirms that contrary to what has been predicted theoretically in various elastic models, undulating layers are fully strained (i.e. not elastically nor plastically relaxed) and can be depicted by the schematic view given in figure 4(c).
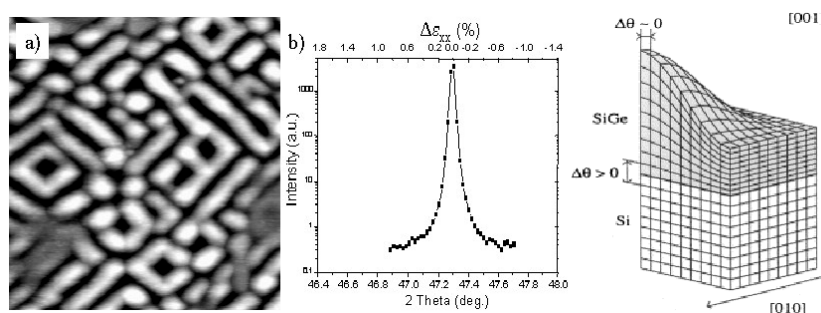
Figure 4. (a) An AFM image of the undulating $Si_{0.7}Ge_{0.3}$ (001) layer and (b) GIXRD θ–2θ scans around the $(2\bar{2}0)$ reflection at $2\theta = 47°3'$ and the $\Delta d/d$ average value in the layer. (c) A schematic representation of the strain distribution in an undulation extracted from CBED measurements.

3.2. Plastic relaxation

Plastic relaxation mechanisms have been the subject of extensive work [9–15] and are beyond the scope of this paper. However, in order to clarify the relaxation behaviour on Si(111) and (001), we will briefly recall the basic equation of the critical thickness (h_{cr}). The latter is defined as the thickness at which it becomes energetically favourable to relax the stress by introducing MD in the heteroepitaxial thin film. The h_{cr}-calculation [16, 17] is based on an energetic balance between the elastic energy per unit area of a biaxially stressed coherent film and the dislocation energy per unit area of an incoherent film. It is commonly described by the Matthews and Blakeslee model [16]:

$$h_{cr} = \left(\frac{b}{8\pi} \right) \frac{(1 - \nu \cos^2 \theta)}{(1 + \nu)\epsilon \cos \lambda} \ln\left(\frac{\alpha h_{cr}}{b} \right)$$

where θ is the angle between the dislocation line and its Burgers vector, b, λ is the angle between the slip direction and the direction in the film plane which is perpendicular to the line of intersection of the slip plane and the interface, α is the core energy parameter. It should be remarked here that this model only describes the propagation of pre-existing threading dislocations, assumed to be present in the substrate, which is not a realistic case. However, up to now, this model provides a better fit of h_{cr} than all the models based on the calculation of the energy of homogeneous dislocation nucleation.

Two different kinds of MD have been experimentally evidenced by high-resolution electron microscopy (HREM) analyses [10] on the two nominal orientations Si(111) and Si(001): a 90° Shockley partial $(a/6)\langle 112 \rangle$ dislocation and an undissociated $(a/2)\langle 110 \rangle$ dislocation respectively. Let us first compare the experimental (h_{exp}-) and theoretical (h_{cr}-) values on the two orientations (001) and (111) in the case of $Si_{0.7}Ge_{0.3}$ ($m = 1.2\%$) grown at 600 °C. The calculated values are $h_{cr} \sim 8$ nm and ~ 12 nm on (001) and (111) respectively while the experimental values are found to be much larger: $h_{exp} \geqslant 50$ nm) [8], and approximately the same on the two orientations. These discrepancies between theoretical predictions and experimental results are explained by the kinetic barrier to dislocation nucleation: in the MB model, MDs nucleate from the propagation of threading dislocations already present in the substrate while in the experiments they nucleate in the epitaxial film on point defects. The discrepancies tend to decrease at high misfit (stress-driven regime) and to increase at low misfit (kinetically driven regime). For instance, $Si_{1-x}Ge_x$ samples with $x = 0.035$ ($m = 0.14\%$) and $x = 0.042$ ($m = 0.17\%$) grown at 600 and 750 °C were studied by means of x-ray techniques. The samples are flat and fully strained (relaxation <5%). A reflection x-ray topograph was used to image individual
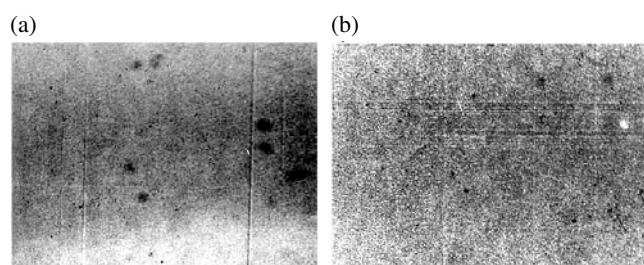
Figure 5. An MD array visualized by reflection x-ray topography with $g = 224$; (a) $x = 0.035$, $h = 800$ nm, $T_g = 600\,°\text{C}$ and (b) $x = 0.042$, $h = 180$ nm, $T_g = 750\,°\text{C}$
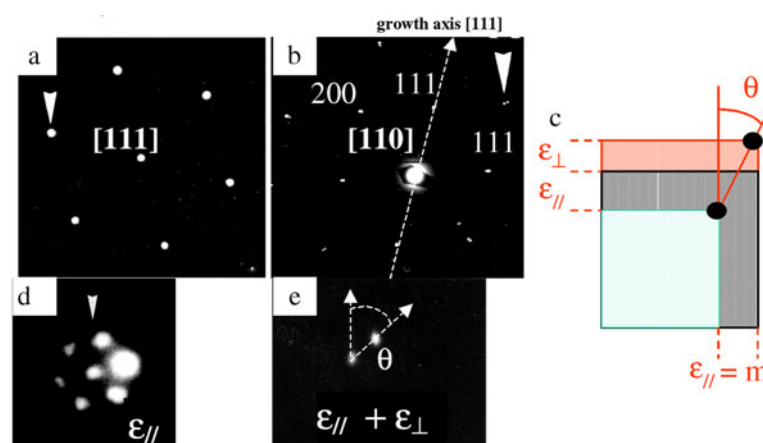

Figure 6. (a) Plan-view and (b) cross-section TED patterns of a 40 nm thick pure Ge layer deposited on Si(111). (c) is the schematic representation of the cell relaxation and (d) the TEM cross-section image of the 3D layer.

MDs and to determine the critical thickness [18] (figure 5). The results summarized in table 2 show that at $600\,°\text{C}$, for $x = 0.035$ the onset of MD nucleation occurs at $h_{exp} \geqslant 800$ nm (~ 8 times larger than h_{cr}) while at $750\,°\text{C}$ for $x = 0.042$ it occurs at ~ 180 nm (~ 2 times larger than h_{cr}). The dependency of h_{cr} on the growth temperature is primarily explained by the kinetics of the relaxation inhibiting the formation of the MD arrays [19]. Moreover, it has been shown that the first source of MDs is the density of dislocations already present in the substrate. This means that when the substrate is free of dislocations the nucleation of MD is delayed.

In order to realize well-controlled two-dimensional electron and hole gas properties in Si–Si$_{1-x}$Ge$_x$ heterostructures with smooth surface morphology, the idea is to grow a fully relaxed buffer layer matching the lattice parameters of the substrate and of the active region. First, the simplest experiment is to grow thick Si$_{1-x}$Ge$_x$ layers. However, it does not permit one to fully relax the stress nor to obtain a smooth surface morphology (to pursue the processing of the layer). For instance the level of relaxation observed in the case of pure Ge/Si(111) (figure 6) has been estimated as $\sim 77\%$ by measuring the parameters parallel and perpendicular to the growth direction ($\varepsilon_{\parallel} \sim 2.6\%$ and $\varepsilon_{\perp} \sim 3\%$).

Another example of a 1 μm thick layer (with Ge concentration $x \sim 0.25$) grown on Si(111) is presented in figure 7(a) [20]. After growth, the surface exhibited a triangular cross-hatch along the three $\langle 110 \rangle$ directions with a roughness of 2.2 nm. The TEM cross-section image (figure 7(b)) evidences the bunching of the threading dislocations to form stacking faults
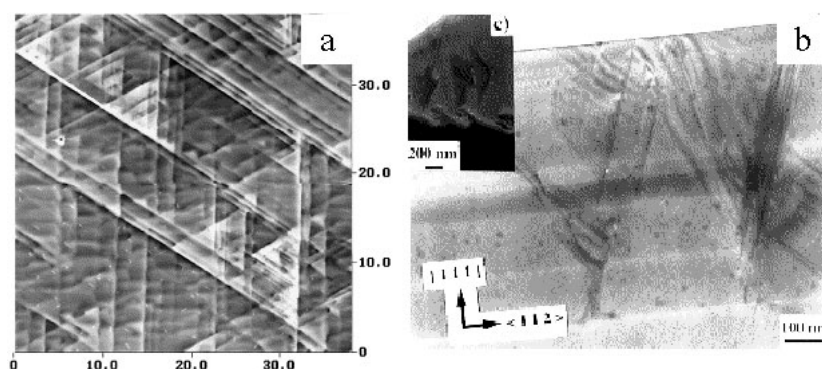
Figure 7. A relaxed $Si_{1-x}Ge_x$ 1 μm thick buffer deposited on Si(111). (a) Surface morphology. (b), (c) TEM cross-sections of the threading dislocations bunched to form stacking faults appearing as bright and dark lines in plan view.

Table 2. Characteristics of $Si_{1-x}Ge_x$ layers with low Ge content.

Ge concentration, x	Tg (°C)	h_{cr} (nm)	h_{exp} (nm)	MD density (cm^{-1})	Relaxation rate (%)
0.35	600	105	170	$<10^{-1}$	<5
0.35	600	105	800	<10	<5
0.42	750	84	180	$<10^2$	<5

($\sim 7 \times 10^8$ cm^{-2}). This prevented the dislocations from gliding further to increase the misfit segment length. Moreover, these stacking faults induced step bunching on the surface.

A more promising approach is the so-called virtual substrate graded composition $Si_{1-x}Ge_x$ layer, which uses thick $Si_{1-x}Ge_x$ films (~ 1 μm) of increasing Ge concentration and greatly reduces the dislocation density in the top-layer region. The film studied was grown at 600 °C and consisted of an initial 400 nm layer with 5% Ge followed by three 200 nm steps of increasing Ge content up to 20% and capped with a 200 nm 18% Ge constant composition layer. XRD measurements performed on this sample showed that the residual strain variation over the sample was negligible. Unfortunately this process also leaves a poor surface morphology (cross-hatch pattern) with an rms roughness of 4.7 nm which is generally believed to come from the dislocation gliding and the strain field of the dislocation in the virtual substrate region (figure 8(a)).

On another sample, Ge islands having a density of 3×10^9 cm^{-2} were pre-deposited to act as nucleation centres for dislocation loops and multiplication sources as well as pinning points for the threading dislocations (2×10^8 cm^{-2}) or for the misfit segment at the interface with the substrate [20]. The cross-hatch was less ordered (figure 8(b)) and the number of threading dislocations had increased. However, no significant change was observed in the rms roughness (4.7 nm). For comparison, the morphology of a sample consisting of a $\sim$500 nm thick $Si_{1-x}Ge_x$ layer deposited on the top of a thin silicon layer pre-deposited at LT on the substrate is presented. It can be seen (figure 8(c)) that the latter process permits us to considerably reduce both the surface roughness (rms $\sim$1.1 nm) and the density of dislocations ($\sim 5 \times 10^4$ cm^{-2} as extracted from AFM images). This is explained by the presence of numerous point defects in the LT Si layer that act as nucleation centres for dislocations. Indeed, it is clearly shown in the cross-section TEM image that most of the dislocations nucleate at the Si substrate/LT Si layer interface (figure 8(d)). Moreover, the pinning of MDs is also evidenced by the absence of threading dislocations in the top layer of the $Si_{1-x}Ge_x$ layer.
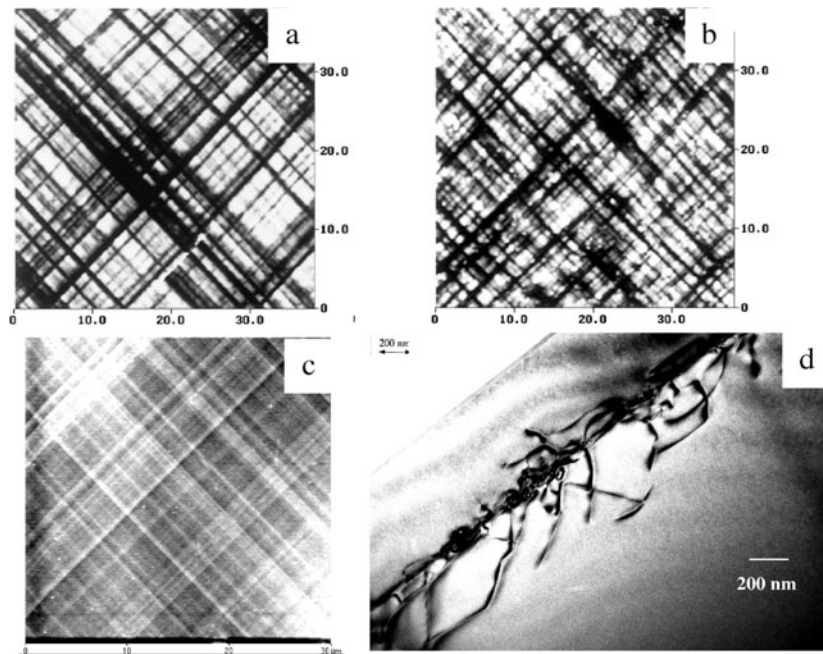
Figure 8. An AFM comparison of the surface morphology of relaxed buffer layers obtained in the following conditions: (a) a graded layer directly grown on the substrate; (b) a graded layer grown on pre-deposited Ge islands; and (c) an SiGe layer grown on a pre-deposited low-temperature (LT) Si layer. (d) The TEM cross-section image of (c), where pinning of MDs and propagation in the Si substrate are shown.

Various mechanisms have been proposed to explain the surface cross-hatch formation. Because of the lattice mismatch between the layer and the substrate, dislocations are introduced in the layer at the growth front [21, 22] and propagate to the epilayer/substrate interface where misfit segments are formed whose edge component relieves the strain accumulated in the layer. Due to the low strain inside the layer, it is favourable for the two threading dislocations associated with the misfit segment to glide in order to increase the misfit segment length rather than nucleate new dislocations. Whilst gliding, the misfit segments interact with each other to create low-energy sources for the introduction of new dislocations [23, 24]. During this movement, there is bunching of misfit segments which have the same Burgers vector [25].

Moreover we have shown that

 (i) the threading dislocation density has no influence on the surface morphology and that
(ii) it is only the mean misfit segment length that is responsible for the cross-hatch morphology.

Surprisingly, a much lower roughness was observed on the (111) substrate compared to that on (001). We believe that the lower surface energy of the (111) surface is responsible for the low roughness, as already proposed for the action of hydrogen on the surface roughness in GSMBE or for growth on (118) surfaces [26].

We have shown unequivocally that the cross-hatch is not related to the threading dislocations, but only to the misfit dislocation length in the layer [20]. The surface free energy then determines the amplitude of the cross-hatch. In conclusion, the realization of new devices based on such relaxed buffer process will need further work before use.
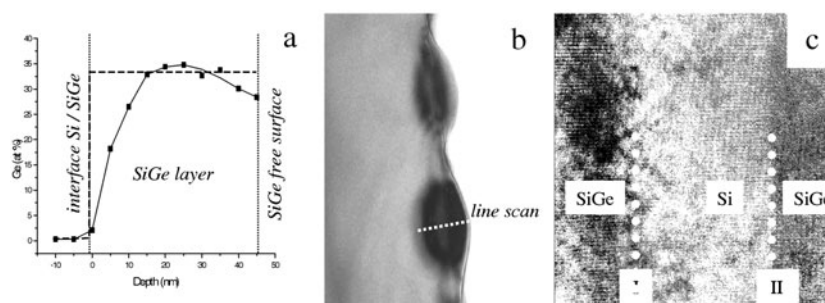
Figure 9. (a) Local Ge concentrations as obtained by EDS analyses performed along a cross-section line from the Si/SiGe interface towards the topmost SiGe layer shown on the TEM cross-section in (b). (c) A TEM cross-section of the Si/SiGe interfaces of a multi-layer sample. The diffraction contrast evidences the interdiffusion at the SiGe/Si interface (I) being higher than that at the Si/SiGe one (II).

3.3. Elastic relaxation

Two elastic relaxation events take place during $Si_{1-x}Ge_x$/Si growth when the elastic energy stored in the layer becomes high enough but just before the onset of plastic relaxation by nucleation of MDs: 'chemical relaxation' by strain-enhanced interdiffusion of Ge/Si and 'step edge relaxation' in 3D islands.

The first mechanism is well known but often difficult to accurately measure. Regarding the deposition of pure Ge on Si at 550 °C (see figure 5) we were able to deduce a Ge concentration ~ 0.79 (from $\varepsilon_\parallel + \varepsilon_\perp \sim 3.35\%$) far below the nominal one. This strain-enhanced interdiffusion mechanism is reduced for layers with lower Ge concentration. For instance, in undulated $Si_{1-x}Ge_x$ layers (with $x \sim 0.3$), the maximum Ge concentration (figure 9(a)) extracted from EDS line scan analyses (figure 9(b)) was found to be in agreement with the nominal one ($x \sim 0.33$). However, the Ge concentration profile presents a maximum located at about the mid-depth of the layer and the $Si/Si_{1-x}Ge_x$ interface extends over ~ 15 nm. This is very detrimental for the fabrication of many devices that need abrupt interfaces. Moreover, the lower Ge concentration at the top surface is explained by the native silicon dioxide. When the $Si_{1-x}Ge_x$ layer is buried by a Si cap layer, the resulting Ge concentration is commonly lower than the nominal one. This reduction is due to the strain-enhanced Si/Ge interdiffusion in conjunction with the dynamic segregation of Ge during growth. We have shown that Si/Ge interdiffusion can be almost completely suppressed in 3D $Si_{1-x}Ge_x$ islands, when the interruption times between the growth of $Si_{1-x}Ge_x$ and Si cap layers are sufficiently long [27]. This was explained by the stabilization of low-energy facets that reduce the surface energy of the islands and maintain their shape/composition. Finally, because of the dynamic segregation of Ge during growth the interface $Si_{1-x}Ge_x$/Si layers are broader than the $Si/Si_{1-x}Ge_x$ ones. This is evidenced by the diffraction contrast of TEM images (figure 9(c)) in which interface I appears broader than interface II.

The second mechanism is the elastic relaxation at the step edges of the 3D islands. This has been measured by means of XRD in the case of $Si_{0.7}Ge_{0.3}$ islands [28]. The results presented in figure 10 show that:

 (i) no lateral elastic strain ($\varepsilon_{xx} \sim 0$) is observed in 2D undulated layers at $h = 5$ nm;
 (ii) about 16% elastic relaxation ($\varepsilon_{xx} \sim 2 \times 10^{-3}$) is reached in 'hut' islands with rectangle-based shape at $h = 10$ nm; and
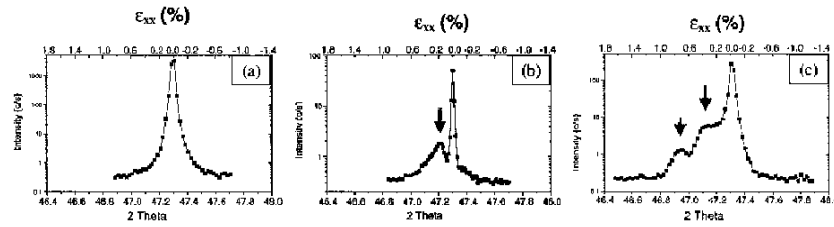(iii) about 70% elastic relaxation ($\varepsilon_{xx} \sim 8 \times 10^{-3}$) is reached in large 'dome' islands.

Figure 10. GIXRD θ–2θ scans around the Si($2\bar{2}0$) reflection at average values of $2\theta = 47.3°$ ($\lambda = 0.154\,05$ nm) and ε_{xx} for Si$_{0.7}$Ge$_{0.3}$(001) (a) as-grown layers with $h \sim 5$ nm, (b) as-grown layers with $h \sim 10$ nm, and (c) annealed layers with $h \sim 5$ nm. The arrows indicate the peaks corresponding to (partially) relaxed structures.

In the detection limit of TEM observations, all the samples studied in this set of experiments were free of dislocations. The two levels of elastic relaxation observed in the two latter cases are attributed to different island shapes. This could explain the first-order shape transition between 'hut' and 'dome' islands (see section 4.2).

4. Nucleation, growth, and self-assembly processes

4.1. Introduction

It is commonly reported that self-assembling of QDs goes through the classical stages of nucleation and growth of islands followed by a last sequence of coarsening (Oswald ripening or other diffusive mechanism) [28]. This part of our review summarizes the current status of research in the field of nucleation, growth, and self-organization for Si$_{1-x}$Ge$_x$ QDs. Particular attention is paid to comparison of the Si$_{1-x}$Ge$_x$ surface evolution on Si(111) and that on Si(001). In particular, we report a systematic investigation of Si$_{1-x}$Ge$_x$ island morphologies that form in between the 2D–3D growth transition (with the exception of dislocated-induced morphologies).

The deposition of pure Ge on Si is commonly described as a classic Stranski–Krastanov (SK) process. It has been recently shown that the growth on (001) is considerably more complex than the simplified SK growth observed on (111). Briefly, Ge deposition on (001) can be summarized as follows [30–33]. In a first stage, growth proceeds in a layer-by-layer mode characterized by a fast increase of the ML step density and the formation of dimer vacancies that order in a $(2 \times n)$ reconstruction. 3D islands start to form just after this surface roughening, probably using the micro-roughness as nucleation centres [34]. As coverage continues to increase, different temperature-dependent metastable morphologies occur (hut clusters, domes, . . .), that finally undergo a phase transition towards very large ($\phi \geqslant 1\ \mu$m) dislocated islands [35]. However, in this scheme of growth, the origin of the first stage of roughening is still under debate (kinetic or stress-driven instability). Also, the origin of the formation of hut islands and the transition from huts to domes are matters of controversy. Finally, usual models do not consider the role of the orientation and of the atomic configuration of substrates (surface diffusion anisotropy for instance) in the shape of the deposited layers.

Moreover, although there exist extensive theoretical and experimental studies on the strain relaxation mechanisms [30, 36–45], the influence of the substrate orientation on these mechanisms has been poorly investigated [46–48].

In our experiments the Si$_{1-x}$Ge$_x$ deposited thickness was adjusted to maintain the structures in metastable states (see figure 11), just below the critical thickness of dislocation nucleation (h_{cr}) but higher than the theoretical critical thickness for islanding (H_{cr}).
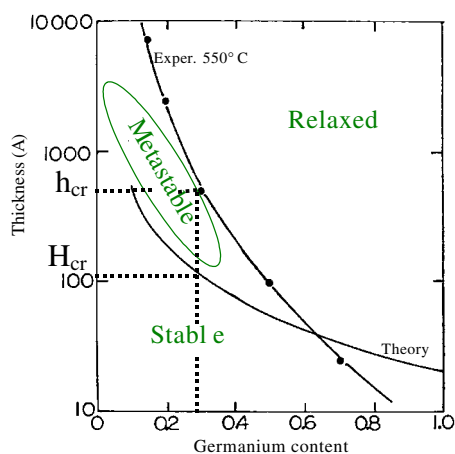
Figure 11. A schematic representation of the different regimes (strained, metastable, and relaxed) of Si$_{l-x}$Ge$_x$ growth as a function of the thickness and of the Ge concentration.
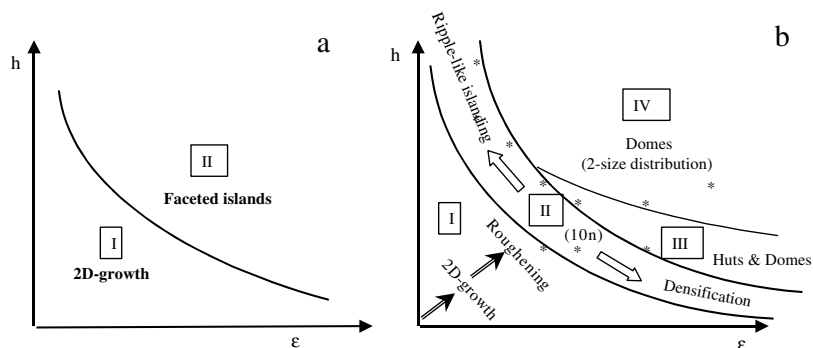

Figure 12. The kinetic phase diagram (at $Tg \sim 550\,^\circ\text{C}$) representing the main growth regimes as a function of the deposited thickness (h) and the misfit (ε): (a) on Si(111) and (b) on Si(001).

4.2. Kinetic phase diagram

In practice, even if the critical thickness of stress relaxation is the same on (001) and (111) surfaces [7, 49], huge differences are found in the kinetics of the 2D–3D growth transition. In particular, the island formation and evolution are very different on (001) and (111), (001) being unique in exhibiting the formation of metastable coherent (dislocation-free) islands. In fact, all the metastable states observed on (001) are completely inhibited on (111). This was reported by us in [50]. In order to summarize the behaviour on both orientations, kinetic phase diagrams of surface morphologies as a function of the two most relevant parameters (the deposited thickness h and the misfit ε) are presented in figure 12 [51]. They have been extracted from systematic investigations of as-grown Si$_{1-x}$Ge$_x$ surfaces that occurred, in our growth conditions, by a competition between kinetic (step flow growth and very high supersaturation) and thermodynamic processes.

On Si(111) only two growth regimes can be distinguished: 2D layer-by-layer growth at low (h, ε); and classical SK growth at high (h, ε). In the latter case plastically relaxed islands that present large facets oriented along (113) and (111) have been obtained [7]. Undulations and dislocation-free islands were never observed on this substrate orientation.
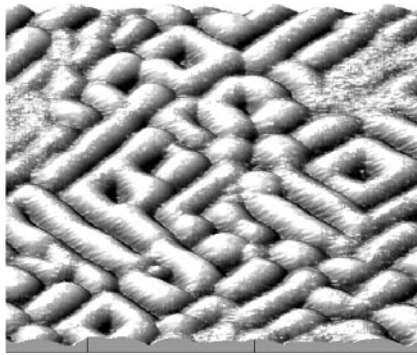
Figure 13. An AFM image of undulations elongated along $\langle 100 \rangle$ and $\langle 010 \rangle$ directions obtained in regime I for $Si_{0.85}Ge_{0.15}$ ($h = 100$ nm).

On (001) the evolution of $Si_{1-x}Ge_x$ surfaces is quite different and can be broken into four main regimes:

- *Regime I* is characterized by a layer-by-layer growth accompanied by a gradual increase of surface roughness which primarily consists of dimer vacancies [52], kinks, and additional steps [53, 54]. Vacancies are assumed to serve as a strain-relief mechanism [29, 33]. At sufficiently high density of vacancies they order to form the $(2 \times n)$ reconstruction which presumably further reduces the strain energy. Even if surface roughness increases very rapidly in this regime, the steady-state morphology is characterized by a succession of S_A and S_B steps oriented along the $\langle 110 \rangle$ directions. A comprehensive review on quantitative scanning tunnelling microscopy (STM) analysis of surface roughening during submonolayer growth of Ge on Si(001) can be found in [33].

- *In regime II*, ripple-like islands (or undulations) that exhibit a broad distribution in size and in shape are observed at low (h, ε). The striking feature of these ripple-like islands is their side orientation along $\langle 100 \rangle$ directions. Furthermore, at increasing thickness they elongate in chains or in square patterns oriented along [100] and [010] (figure 13). They present very small aspect ratios ($h/L \sim 0.03$) and side angles of about $\sim 5°$ (instead of $11.3°$ for (105) facets) without extended facets on their sides.

  Such undulations are fully strained [7] ($\Delta \varepsilon_{xx} \sim 0$ was found by both CBED and GIXRD). The kinetics of ripple-like island formation along the $\langle 100 \rangle$ directions, i.e. at 45° from the $(2 \times n)$ reconstruction rows, is still unclear. It turns out that such morphologies can be equilibrium structures of (001) surfaces subjected to biaxial compressive stress [54, 55] but it is evident that kinetic considerations [56–59] cannot be ignored since kinetic instabilities observed in Si homoepitaxy [60–63] give rise to similar morphological evolution of layers (see section 4.3).

  At higher misfit ($\varepsilon = 1.2\%, x \sim 0.3$), square isotropic mounds (with lateral size $L \sim 100$ nm) nucleate, superimposed on the rough surface. These islands, usually called 'huts', adopt pyramidal shape with the four bases oriented along $\langle 100 \rangle$ directions and the four facets approximately corresponding to (105) facets [30]. GIXRD analysis proves the absence of elastic relaxation in such 'hut' islands [28]. In this regime, their morphological evolution with the thickness differs from their evolution with the misfit (figure 14). Indeed, at increasing deposited thickness, there occurs a shape transition from square-based islands (figure 14(a)) to elongated rectangle-based islands (figure 14(b)), while an increasing

misfit induces an increasing density of square-based islands. In fact the intersection point between regimes II, III, and IV represents an experimental compromise between density, size, and homogeneity of islands. Figure 14(c) gives an example of the $Si_{1-x}Ge_x$ islands obtained in these experimental conditions (density $\sim 2 \times 10^{10}$ cm^{-2}).

In order to determine the stability of such 'hut' island shape, we have followed their morphological evolution during an annealing at 550 °C [51]. Starting from a ripple-like as-grown surface, formation of fully strained 'hut' islands occurred after 1 h 30 min annealing (no elastic relaxation was detected at this stage). After 18 h annealing, islands evolved towards large isolated 'huts' that exhibited well-defined (105) facets (figure 14(d)). Elastic relaxation measured in these large hut islands ($\Delta\varepsilon_{xx} \sim 0.25\%$) is very low. They are consequently still highly strained (about 0.75%).

No further evolution (of the morphology and of the elastic relaxation) occurred during the following 46 h annealing. This proves that large 'huts' represent an equilibrium steady state and we suggest that their morphology is stabilized by the compressive biaxial stress applied by the substrate to the islands. If this is the case, (105) facets would be expected to have lower surface energy than (100) facets under compressive stress. Thermal stability of hut islands (during long-term annealing) was also reported in [64]. However, this is in contradiction with the conclusions of [32, 65] which state that huts only provide a kinetically favourable path from 2D to stable macroscopic islands. In our scheme of growth, these results that seem contradictory are in fact compatible, as will be shown below (see the *regime III* description). Nevertheless, further experiments are needed to determine the exact origin of hut island formation (minimization of (105) surface energy under compressive stress).

- *In regime III*, coexistence of 'huts' and 'domes' is observed (figure 15(a)) [66, 67]. The two island groups are characterized by different aspect ratios (~ 0.15 and ~ 0.04 for 'domes' and 'huts' respectively) and different shapes: pyramidal 'huts' that have been described previously (figure 15(b)) and round-shaped 'domes' (figure 15(c)) with the larger facets corresponding to {113} and {111} planes (figure 15(d)). Several other side orientations were found at the top of the domes, but they could not be accurately determined. For a detailed description of the dome shape, see [66]. The respective densities of 'huts' and 'domes' varies with the experimental conditions: 'domes' are favoured in the higher-stress regime, while 'huts' are favoured in the lower-stress regime. The most striking result here is that a much higher level of elastic relaxation was measured in 'domes'. For instance, $\Delta\varepsilon_{xx} \sim 0.78\%$ was found in an as-grown $Si_{0.5}Ge_{0.5}$ layer with $h = 5$ nm ($\varepsilon = 2.1\%$).

  In this growth regime, as-grown square islands also transform during annealing (long-term annealing at 550 °C) into larger round-shaped domes that constitute the steady-state morphology of this growth regime. This transition, based on a ripening process, is accompanied by a dramatic increase of the relaxation level ($\Delta\varepsilon_{xx} \sim 0.85\%$) [51]. This suggests that the 'hut'/'dome' transition is mainly driven by stress relaxation and that hut islands (and in particular (105) facets) are destabilized by the elastic stress relaxation. As a consequence, as the stress relaxation takes place, the (105) facets decrease in size at the expense of (113) and (111) facets that are the low-energy facets present in the equilibrium shape of bulk Si (without stress). In this scheme of growth each step accompanied by stress relaxation will induce the hut/dome transition. For instance, at an intermediate level of misfit (compressive stress), the islands are highly strained (low stress relaxation) and the (105) facets have low surface energy. Huts represent the steady-state morphology of this regime. At higher misfit, because stress relaxation is energetically favoured (elastic relaxation or dislocation nucleation) the islands are largely relaxed and the steady-state morphology then consists of domes. So, even if the formation of huts is possible during growth, they represent kinetic pathways in this stress regime and will rapidly transform into domes, during
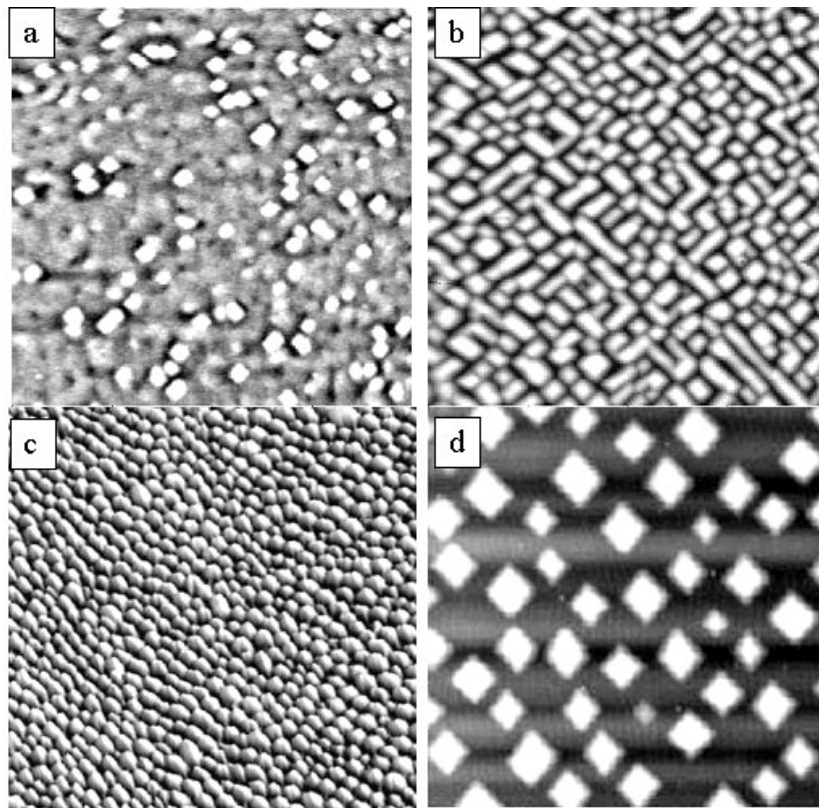
Figure 14. AFM images (scan size $2\mu x 2\mu$) of $Si_{1-x}Ge_x$: (a) as grown 'hut' islands with $x = 0.3$ and $h \sim 5$ nm; (b) as grown 'hut' islands with $x = 0.3$ and $h \sim 10$ nm; (c) as grown 'hut' islands with $x = 0.35$ and $h \sim 5$ nm; (d) 'hut' islands with $x = 0.25$ and $h \sim 10$ nm stabilised during 18 h annealing at 550 °C.

any annealing. We suggest that this could explain the contradictory results reported above.

- *In regime IV*, a bimodal size distribution of domes is observed. They correspond to dislocated and coherent structures. The latter ones are similar to those described in the previous section. Hut islands are never observed in this regime. The steady-state morphology consists of larger-sized relaxed islands. Such islands are not relevant for this paper. For a comprehensive review on the dislocation nucleation, see [13, 14].

4.3. Growth instability

We have seen in section 4.2 that on Si(001), regime II is characterized by the development of instabilities (undulations) that lead to a sinusoidal-like morphology. The evolution of such instabilities during epitaxial growth on Si surfaces has been of increasing interest over the past few years for two opposite reasons. First, because any corrugation of the SiGe surface is very detrimental in the fabrication of high-speed electronic devices that require abrupt interfaces and flat layers. Second, because in contrast, periodic sinusoidal morphology can be used as self-patterned templates for selective growth of self-assembled nanostructures (see section 4.4).
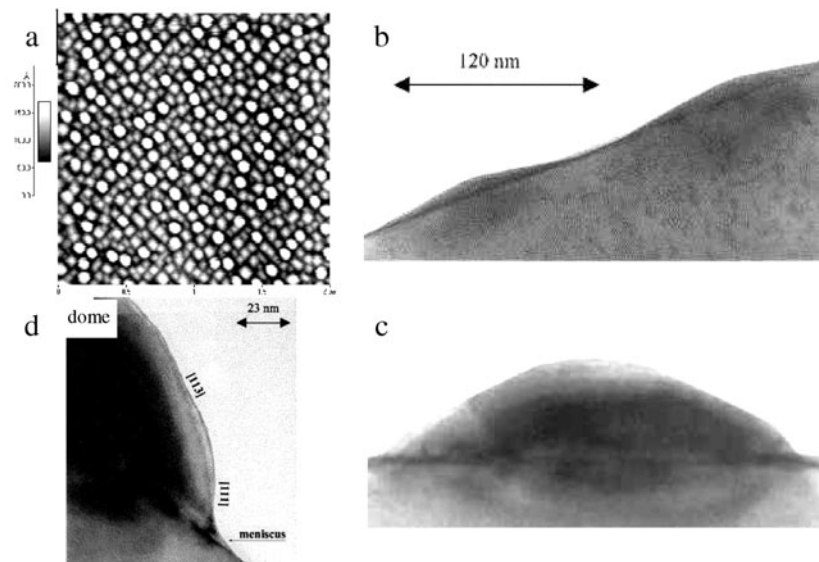
Figure 15. (a) An AFM image of the bimodal size distribution of islands due to the coexistence of square-based 'hut' and round-shaped 'dome' islands for $Si_{0.6}Ge_{0.4}$ ($h = 5$ nm). TEM cross-section images of (b) 'huts' and (c) 'domes'. The enlargement of (c) presented in (d) evidences the presence of (113) and (111) facets.

In the past, there has been considerable controversy regarding the influence of stress on growth instabilities. The main issue was whether surface undulation favours dislocation nucleation or not. In some cases, the lateral elastic relaxation of the layer on the top of the undulation was proven to lower the amount of accumulated elastic energy inside the heterolayer leading to larger critical thickness of strained pseudomorphic films [13, 38, 39]. In other cases, preferential dislocation nucleation was assumed to be initiated in highly strained local areas in the valley of the undulation [15, 36, 68]. In all cases, the main hypothesis was the existence of a critical wavelength and/or of a critical stress, beyond which the surface becomes unstable with respect to a sinusoidal corrugation [44, 45, 69, 70]. This is the basic idea of the Asaro–Tiller–Grinfeld (ATG) modelling which considers the instability under the formulation of continuum elasticity. The layer becomes corrugated when the excess of surface free energy due to the corrugation and the elastic energy paid by the strain field distribution is compensated by the gain of elastic energy due to relaxation in 3D islands.

In the previous paragraph, we have reported that the growth instability which develops during $Si_{1-x}Ge_x$ growth on Si(001) does not develop on Si(111) in the same experimental conditions. Thanks to deeper analyses [7], this was attributed to the different atomic configurations of the Si(001) and Si(111) surfaces. This dramatic role of the atomic surface morphology and of the kinetics of step motion questions the validity of models based on the elastic relaxation in islands in order to explain the development of growth instabilities. In fact, in order to understand the mechanism, both kinetics (anisotropy of surface diffusion) and atomic arrangement of the surface (surface reconstruction and step edge configuration) should be considered. Hereafter, we investigate the role of step density and of stress on the onset/evolution of the growth instability. We concentrate our investigations on the morphology of Si and $Si_{1-x}Ge_x$ vicinal layers and on the influence of stress on this morphology. We show that different behaviours are observed depending on the nominal orientation of the substrate.
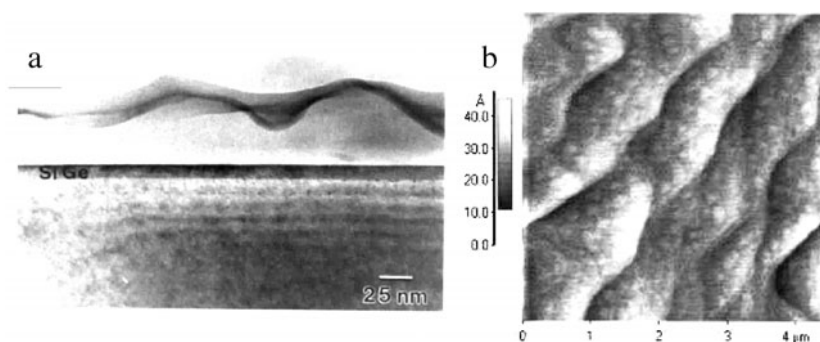
Figure 16. A 10 nm thick $Si_{0.7}Ge_{0.3}$ layer deposited on Si(111): (a) a cross-sectional TEM observation and (b) an AFM image of the surface which exhibits large flat terraces ($\sim$0.2 μm) separated by trilayer steps ($\sim$1 nm height).

4.3.1. Growth on Si(111).

4.3.1a. Singular Si(111). Instability was never observed during the homoepitaxy of Si on nominal Si(111) whatever the deposited thickness (h) was (varying from 100 to 1000 nm) [71]. The growing surface remained free of defects and perfectly flat throughout the growth. Even at $h \sim 1$ μm the layer exhibits a regular single-height (SH) array of steps and large $\sim$0.2 μm terraces.

When a $Si_{1-x}Ge_x$ film is grown on Si(111), the film is biaxially compressed in the growing plane along the $\langle 110 \rangle$ and $\langle 112 \rangle$ crystalline directions. For small h, $Si_{1-x}Ge_x$ grows in a coherent layer-by-layer fashion and exhibits large terraces separated by trilayer steps ($\sim$1 nm height) [71]. Bi-dimensional nuclei are also visible on the terraces (figure 16).

As h increases the elastic energy within the film quickly outruns the dislocation energy making it favourable for forming a partially incoherent structure when h exceeds a critical value h_{cr}. The 2D–3D growth transition never occurs in this range of misfit and the dislocated layers do not have any periodic undulations [7]. However, 2D–3D transition occurs during the Ge/Si growth, leading to dislocated relaxed Ge islands.

4.3.1b. Vicinal Si(111). Initially we studied the homoepitaxial growth of Si/Si misoriented at 2°, 6°, and 10° (in the $[\bar{1}\ \bar{1}\ 2]$ direction) [71]. Just after the *in situ* cleaning procedure preceding growth, the Si misoriented surfaces are composed of regular arrays of tri-atomic steps separated by flat (111) terraces (5.5 nm at 10° off) that exhibit the 7×7 superstructure.

In all cases, for a deposited thickness h lower than 150 nm, we only observe a small kinetic roughness which can be regarded as a Gaussian roughness. For larger h ($\sim$500 nm), a periodic undulated surface stabilizes during growth (figure 17(a)).

HREM observations have shown that one period of undulation (figure 17(b)) can be divided in two main areas: a climbing orientation (a) and a descending one (b). Higher-magnification images (figure 17(c)) show that both orientations (a) and (b) consist of combinations of low-energy facets, (111) and (112). Most of the rising areas (a) comprise (111) facets, while most of the descending areas (b) consist of (112) ones. Consequently the surface profile can be schematically represented by the diagram presented in figure 17(d).

The variations of the amplitude (A) and of the periodicity (λ) are consistent with a kinetic step bunching mechanism: (1) A and λ evolve as t^α and t^β respectively with the deposited thickness—the critical exponents extracted from experiments are $\alpha \sim 0.5$ and $\beta \sim 0.16$;
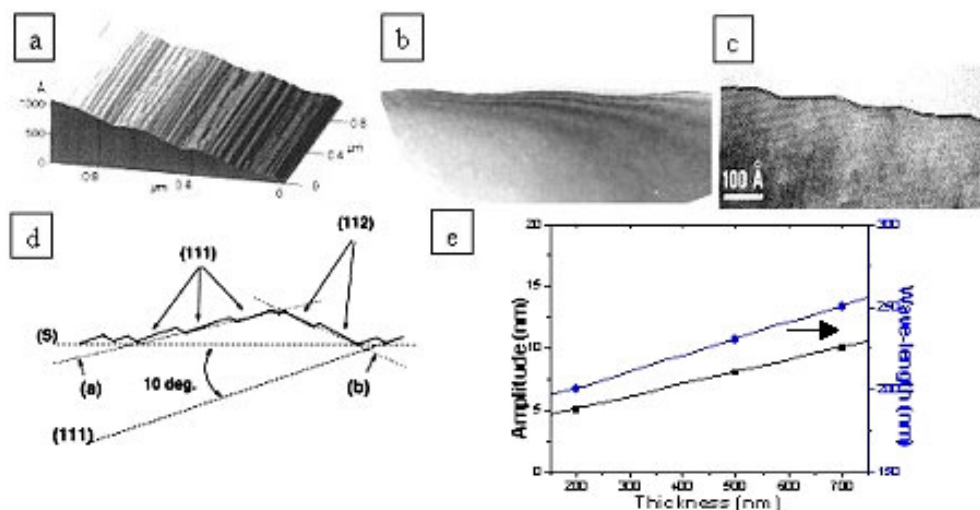
Figure 17. Homoepitaxy of Si($h \sim 500$ nm)/Si(111). (a) An AFM image of the anisotropic undulation. ((b), (c)) TEM cross-sectional images (b) of the periodic undulations and (c) of the local arrangement of the facets. (d) A schematic representation of one period of the undulation deduced from HREM measurements. (e) Morphological evolution of the amplitude (A) and periodicity (λ) of the instability with the deposited thickness.

(2) λ increases with the temperature; and (3) the amplitude maximum of the instability is at $\sim 700\,°$C. The kinetic Monte Carlo simulation of the kinetic instability is in progress.

We then investigated the growth of $Si_{0.7}Ge_{0.3}$ layers when deposited at $2°$, $4°$, $6°$, and $10°$ off Si substrates [28, 71]. We intentionally limited the study to fully strained $Si_{0.7}Ge_{0.3}$ layers (free of defects). The morphological evolution of the layers with the miscut angle (from $2°$ to $10°$) is shown in figure 18. This evolution is consistent with a faceting instability (increase of A and decrease of λ with the miscut angle).

For $2°$ miscut angle, the surface consists of high step bunching (from 3 to 10 ML) aligned along $\langle 113 \rangle$ directions, leading to triangular shape. With increasing miscut angle, the triangular shape elongates along the direction of misorientation which is the direction of the step edges. At $10°$ off, the surface exhibits large anisotropic periodic undulations with a typical asymmetric shape. λ has been estimated from AFM analysis to be in the micrometre range and A to be about 8 nm. In a similar manner to that for Si layers, TEM cross-section analysis evidences the onset of (111) and (113) facet formation on the side parts of the undulation.

Regarding the effect of stress, we find that the biaxial compressive stress applied to the growing film during $Si_{1-x}Ge_x$ heteroepitaxy dramatically enhances the instability development. Indeed, for instance at $10°$ off Si(111) the morphology of a 500 nm thick Si layer is comparable to those of a $Si_{1-x}Ge_x$ ($x = 0.3$) layer 10 nm thick obtained in the same experimental conditions. Moreover, faceting is more developed under biaxial compressive stress. We suggest that the onset of the instability could be attributed to a change of the interaction energy between steps and/or to a step edge energy, at a critical step density, due to local stresses at the step edges. The evolution of the phenomenon is then kinetically controlled by various kinetic factors (growth temperature, compositionally enhanced surface diffusion, step edge diffusion anisotropy, ...). In a second step, the periodic morphology, which is a metastable state, kinetically evolves towards a faceted equilibrium shape.
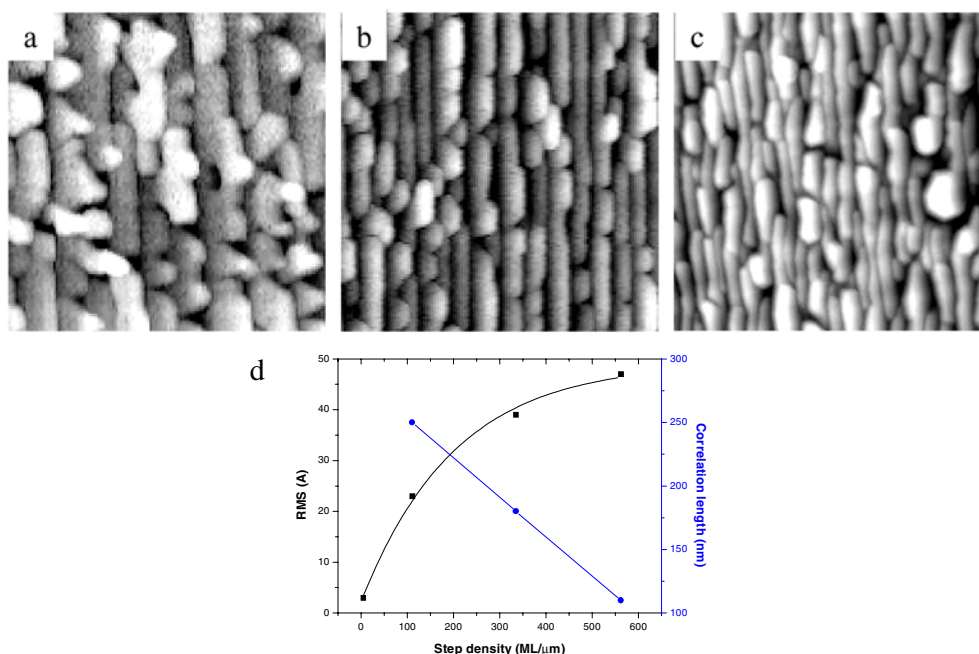
Figure 18. Morphological evolution of 10 nm thick $Si_{0.7}Ge_{0.3}$ layers with the misorientation of the substrate: from $2°$ (a) to $6°$ (b) and $10°$ off (c). In all the images the monatomic steps are vertical. (d) Evolution of the corrugation amplitude (A) and periodicity (λ) with the step density (miscut angle).

4.3.2. Growth on Si(001).

4.3.2a. Singular Si(001). We have seen (section 4.2) that in regime II the $Si_{1-x}Ge_x(001)$ layers deposited on nominally flat substrates exhibit undulated surfaces with more or less isotropic mounds distributed at random on the surface. The origin of these undulations is commonly attributed as a stress-driven growth instability. However, we already observed similar morphologies during the growth of thick Si layers on nominal Si(001) (figure 19).

Moreover, we found in a previous work that the $Si_{1-x}Ge_x$ growth instability varies with

(1) an energetic term which depends on the ratio of surface energy and elastic energy; and
(2) a kinetic term which depends on the ratio of surface diffusion and arrival rate of the species.

In order to determine the influence of terms (1) and (2) on the nucleation and evolution of the surface corrugation we have performed a set of experiments for Ge concentrations varying between $x = 0$ and 0.25. The onset of the instability was related to a critical growth temperature of $\sim600°C$. At LT, the instability did not develop during growth. The $Si_{1-x}Ge_x$ layers were directly relaxed by MDs. This proves that the instability is kinetically driven. At HT, the instability develops for $Si_{0.75}Ge_{0.25}$/Si but not for Si/Si. Its amplitude evolves very abruptly with the deposited thickness (figure 20(d)). As an illustration, the morphology of Si and of $Si_{0.75}Ge_{0.25}\sim500$ nm thick layers deposited on Si(001) at $650°C$ are presented in figure 20. It is obvious that the instability is stress dependent. A typical TEM image of an undulated layer evidences the absence of facets at the surface (figure 20(c)).
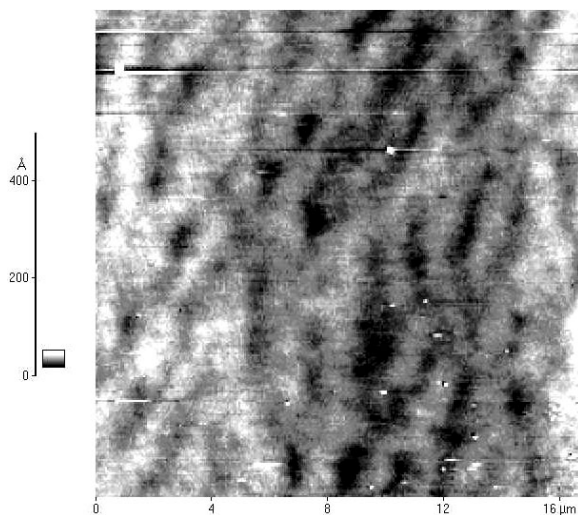
Figure 19. Surface undulation of a ~500 nm thick Si layer when deposited on nominal Si(001) (with miscut <0.5°).

4.3.2b. Vicinal Si(001). In contrast to what was observed on (111), there is no dramatic morphological change induced by the presence of steps on (001). The only difference induced by the misorientation of the substrate is an amplification of the corrugations observed during both homoepitaxy and heteroepitaxy.

In this set of experiments, the miscut angles have been varied between 1.5° off and 10° off in the [110] direction (parallel to the step edge). At LT, a kinetic growth instability develops on vicinal Si(001) during homoepitaxy of Si (in the absence of stress). The corrugation observed presents a maximum amplitude in the transient temperature regime between step flow and island nucleation (figure 21(d)). At this temperature (400 °C and 1.5° off misoriented substrate) the undulation orientates along the pre-existing monatomic steps of the substrate and leads to a periodic ripple-like morphology (figure 21(b)). This instability tends to vanish at HT (figure 21(c)) and to become irregular (step meandering) at LT (figure 21(a)).

Independently of the amplitude, the correlation length of the corrugation continues to increase with the temperature (figure 21(d)) while the instability vanishes. Similar behaviour was observed for step bunching instability which develops during homoepitaxy on vicinal Si(111). Even if the exact physical driving force of the instability is still unknown (inverse Schwoebel barrier, step edge diffusion, . . .), clear evidence of a kinetic growth regime is demonstrated here. Surprisingly, no obvious relation was found between the density of monatomic steps on the substrate (misorientation) and the amplitude/wavelength of the corrugation. Peculiar behaviour of the (118) facet (10° off misoriented surface) could be invoked to explain this result.

Considering now the effect of compressive stress (Ge concentration) on the undulation, it is shown that the kinetic undulation which develops at LT during homoepitaxy is completely inhibited in the presence of stress during heteroepitaxy of $Si_{1-x}Ge_x$ layers, even for low Ge content $x \sim 0.05$ (figure 20). The influence of stress on the kinetic growth instability is not clear, but at least a change of the diffusion and sticking barriers is expected. Kinetic Monte Carlo simulation of growth instability is in progress to clarify this effect. At HT, opposite behaviour is observed: the onset of the corrugation is related to a critical level of stress and the corrugation amplifies with the level of stress. These opposite evolutions of the undulation with
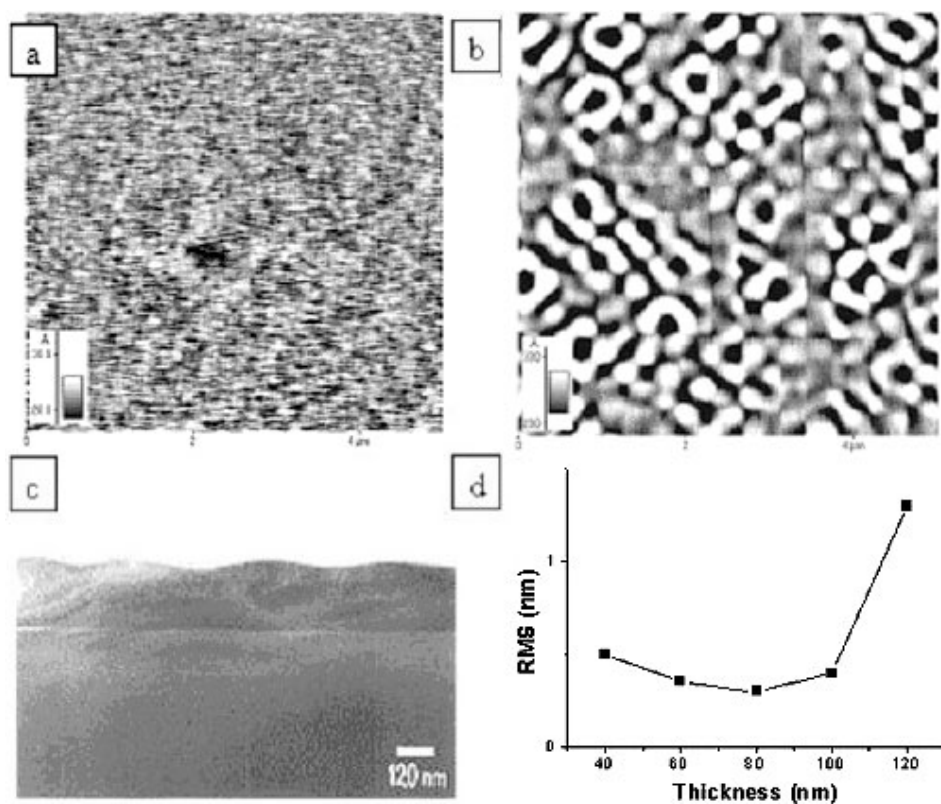
Figure 20. Surface morphology of a $\sim$500 nm thick (a) Si layer and (b) Si$_{0.75}$Ge$_{0.25}$ when deposited on nominal Si(001) (with miscut angle $<0.1°$). [110] is vertical on the two images. (c) TEM cross-section image of the undulated layer of (b). (d) Evolution of the corrugation amplitude of the undulating layer of (b) with the deposited thickness.

stress at two different growth temperatures are reported in figures 22(c) and (d). The evolution on nominal Si(001) is reported as a reference. Similar behaviours are obtained on both 1.5° and 10° off misoriented substrates. These results have not been explained so far.

Let us focus lastly on the morphological evolution of Si$_{0.7}$Ge$_{0.3}$(001) layers with the misorientation angle (figure 23). Different sets of samples were grown by both SSMBE and GSMBE and exhibited similar evolution [28, 72]. The AFM images presented in figures 23(a)–(c) correspond to the samples grown by GSMBE.

The mounds obtained at 0° off remain isotropic up to 4° off. At this value, they elongate perpendicularly to the steps and form triangle-shaped islands (figure 23(a)) that continue to elongate with the miscut angle (from 6° to 10° off). Perfect anisotropic undulations are finally obtained for a 10° miscut angle (figure 23(c)). Surprisingly, this anisotropic undulation extends perpendicularly to the step direction, along [110] in contrast to what was observed on vicinal (111) and in contrast to the kinetic instability observed during homoepitaxy (on both (111) and (001) vicinal orientations). This means that the wire-shaped islands seem to 'ignore' the underlying atomic step distribution and cross over a large number of monolayer or bilayer steps. Consequently, on vicinal (001), the behaviour observed (elongation of the undulation perpendicularly to the pre-existing step edges) cannot be explained by a step bunching mechanism nor by any existing model. In addition, even if the effect of closely
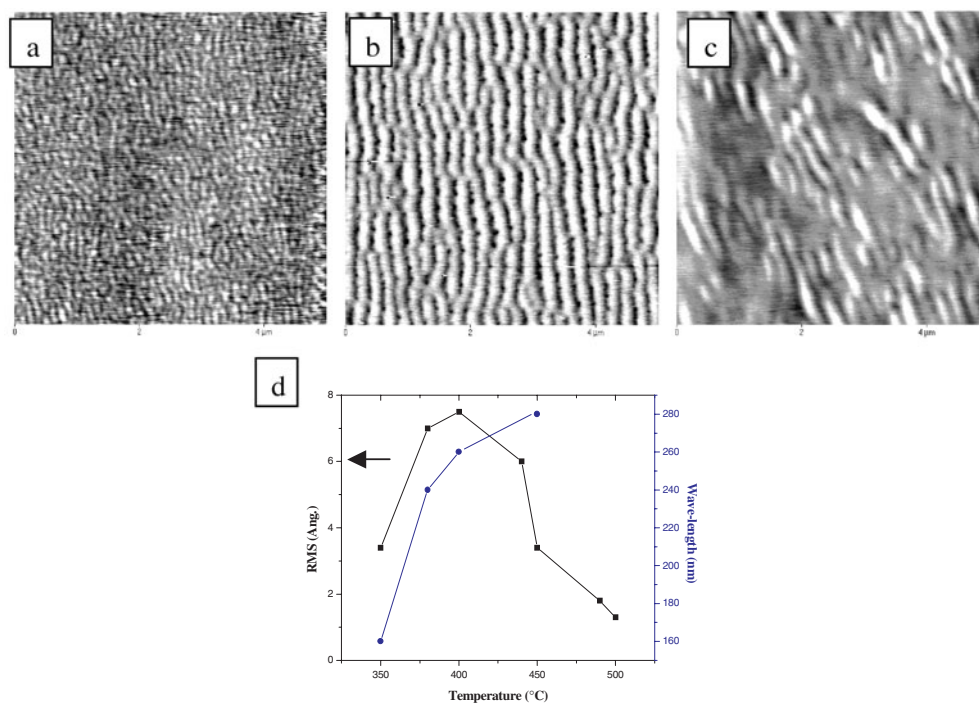
Figure 21. AFM images of 500 nm thick Si deposited on Si(001), 1.5° off, at (a) 350 °C, (b) 400 °C, and (c) 450 °C. In all the images monatomic steps are vertical. (d) Evolution of the corrugation parameters (RMS and wavelength) with the growth temperature.

packed steps (10° off misoriented substrate) outwardly resembles those on both (001) and (111) orientations, the underlying mechanism should be entirely different since undulation orientations are either perpendicular or parallel to step edges. We must note that to check our results we systematically verified the substrate misorientation by Laue diffraction. Another intriguing result is that the wavelength of $Si_{1-x}Ge_x$ undulation remains constant whatever the density of steps (miscut angle) of the substrate. These results have been verified for two different Ge contents (figure 23(d)).

In the end, the problem to clarify is whether the Si/Si and $Si_{1-x}Ge_x$/Si instabilities could be described by a unified model. This would permit one to predict the pattern parameters (amplitude, periodicity, and shape) in relation to the experimental conditions. We suggest that the faster amplification of the corrugation for $Si_{1-x}Ge_x$/Si is more driven by kinetics than by elastic relaxation. This leads to new capabilities for obtaining self-patterned substrates.

4.4. Self-organization processes

Several studies have been dedicated to the fabrication of nanostructures to confine carrier motion in reduced dimensions. The different processes developed to control the size and homogeneity of dots use either the SK growth mode [73–76] or patterning techniques (mainly lithography) [77–80]. In both cases difficulties have been encountered in controlling the aspect ratio A/L (island height over lateral size) of dots and their location/density. Generally inhomogeneous size distributions of dots associated with broadened luminescence have been found. We have used mainly two different processes in order to produce self-organized nanostructures with better A/L control.
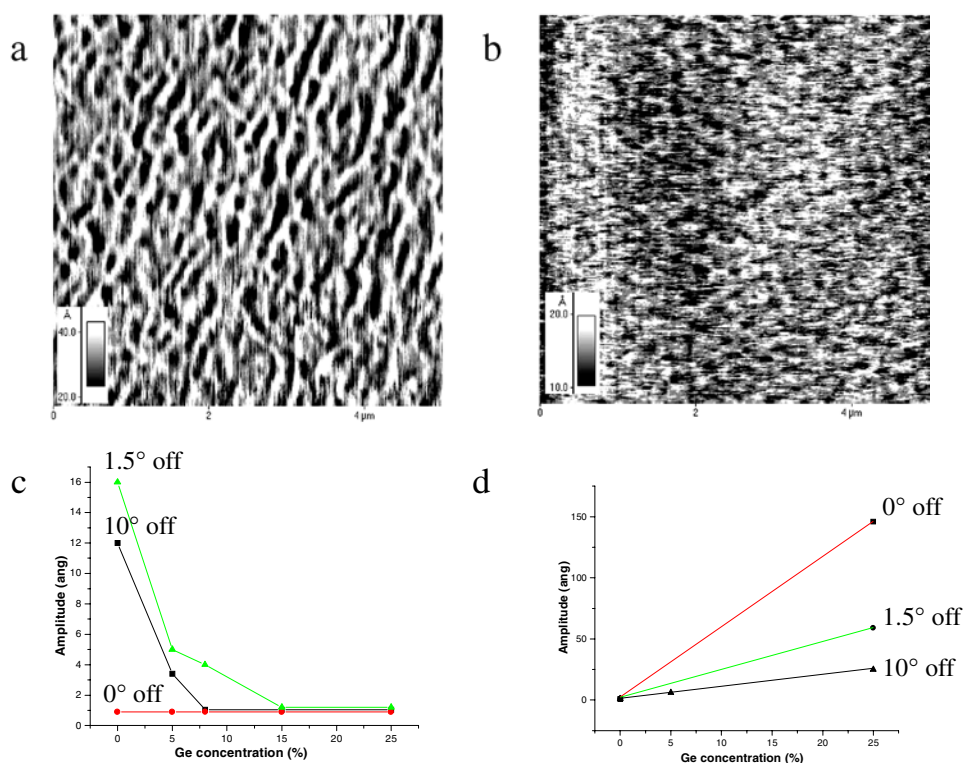
Figure 22. AFM images of ∼500 nm thick (a) Si and (b) Si$_{0.95}$Ge$_{0.05}$ layers deposited at ∼400 °C on Si(001), 1.5° off. (c) and (d) represent the evolution of the undulation amplitude with the Ge concentration at $T_g \sim 400$ and $T_g \sim 650$ °C respectively.

The first process consists of depositing Ge ML on a self-patterned Si$_{1−x}$Ge$_x$ template layer [27, 81]. Self-patterning results from the stress-driven instability detailed upper [7]. The crucial step of this process is selectively growing Ge dots on the top of the periodic pre-patterned Si$_{1−x}$Ge$_x$ (or Si) template layer without affecting the Si$_{1−x}$Ge$_x$ (or Si) undulation wavelength (since undulations could vanish during the Ge post-deposition). Different effects are expected from the template layer: decrease of the Si/Ge interdiffusion, transmission of stress into the Ge dots, creation of kink or step facets on the sides of the undulation, etc. The periodicity and amplitude of the instability were adjusted by varying the kinetics of growth (see section 4.3). The efficiency of the process has been evidenced for 7 ML Ge deposited on the top of a ∼10 nm thick Si$_{0.7}$Ge$_{0.3}$ template layer on Si(001) and Si(001) 10° off orientations [27]. We have shown in particular that A/L could be increased by a factor of 2 by using this two-step process (7 ML Ge deposited on top of a ∼10 nm thick Si$_{0.7}$Ge$_{0.3}$ template layer) and dot homogeneity could also be increased (see section 6 for PL evidence). The major role of the template layer is to control the Ge dot location, as can be seen in the AFM images of figure 24.

The second process of self-organization uses Sb surfactant-mediated growth of Ge on Si(001) [82, 83]. This process has two major effects: it reduces the lateral size of Ge dots and increases their density. Figure 25 shows the evolution with the growth temperature of the Ge surface morphology (thickness ∼1.8 nm) on Si(100) with 1 ML of Sb pre-deposited. First, the different growth modes at 350, 550, and 750 °C are clearly seen. At 350 °C the surface is flat at the level of HREM observation (figure 26). However, the rms surface
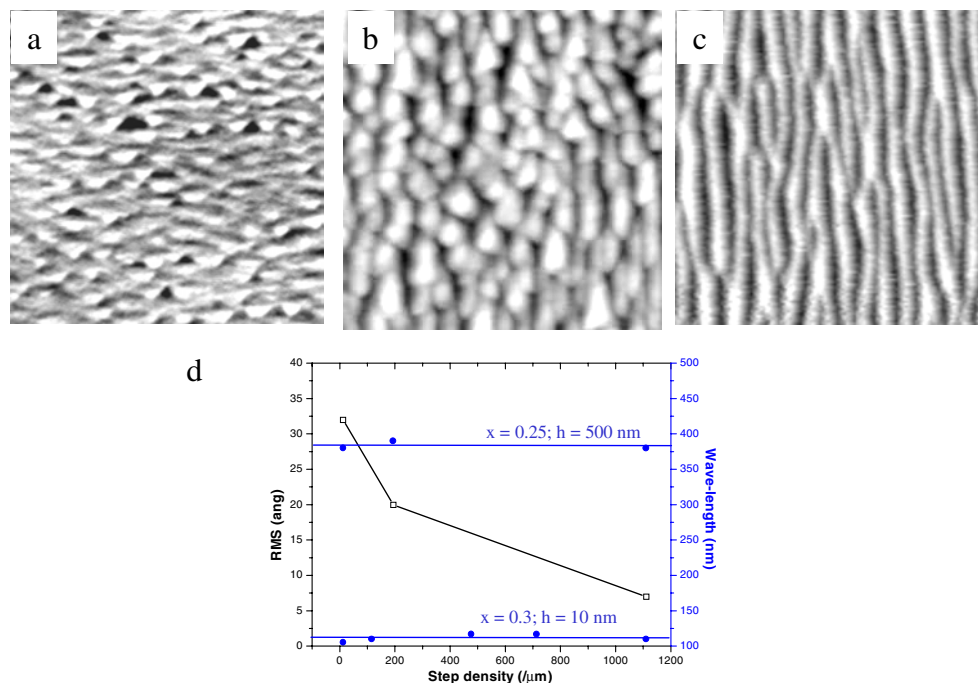
Figure 23. Morphological evolution of 10 nm thick $Si_{1-x}Ge_x$ layers ($x = 0.3$) grown on various Si substrates misoriented from the (001) nominal one: (a) 4° off, (b) 6° off, and (c) 10° off. Monatomic steps are horizontal in all the images.

roughness measured on the AFM image ($\sim$0.5 nm) (figure 25(a)) suggests the onset of 3D island nucleation ($L \sim 20$–30 nm). At 550 °C the formation of ultrasmall dense Ge islands is clearly evidenced (figure 25(b)). At higher temperature, Sb no longer has an influence due to its high rate of desorption from the Si surface. The large isolated islands (figure 25(c)) grown over the flat surface are very similar to those obtained during Ge growth without Sb. This result confirms the total desorption of Sb observed in the literature at this temperature [84–87].

As regards the morphology of the Ge layer grown on a pre-deposited 1 ML Sb, an almost flat layer is obtained at 350 °C (figure 26(a)) while ultrasmall islands of only one type are obtained at 550 °C (figure 26(b)). Due to the small extent of the facets (small lateral size of the islands), it is not possible to determine their exact orientations. However, these islands have a shape very different from those of the huts and domes. HREM images evidence the absence of dislocations in these small islands that are in consequence fully strained.

For comparison, in the same experimental conditions Ge/Si growth without Sb at $T_g = 550$ °C has been followed [82]. It results in the commonly observed bimodal 'huts' and 'domes' island distributions. As a consequence Sb modifies the growth of Ge/Si in different ways. First it delays the 2D–3D transition at LT. This can be explained by the lower surface energy of Sb in comparison to those of both Si and Ge. Another effect is the formation of smaller Ge dots with a higher density during Sb-mediated growth at higher temperature. This can be interpreted on the basis of the reduction of the surface diffusion of Ge adatoms on 1 ML Sb that we have evidenced with RHEED experiments. But it can also be interpreted in terms of stress. Indeed, the level of stress is supposed to be higher for Ge:Sb/Si than for Ge/Si due to the partial incorporation of the larger Sb atoms. Moreover, since SIMS experiments have
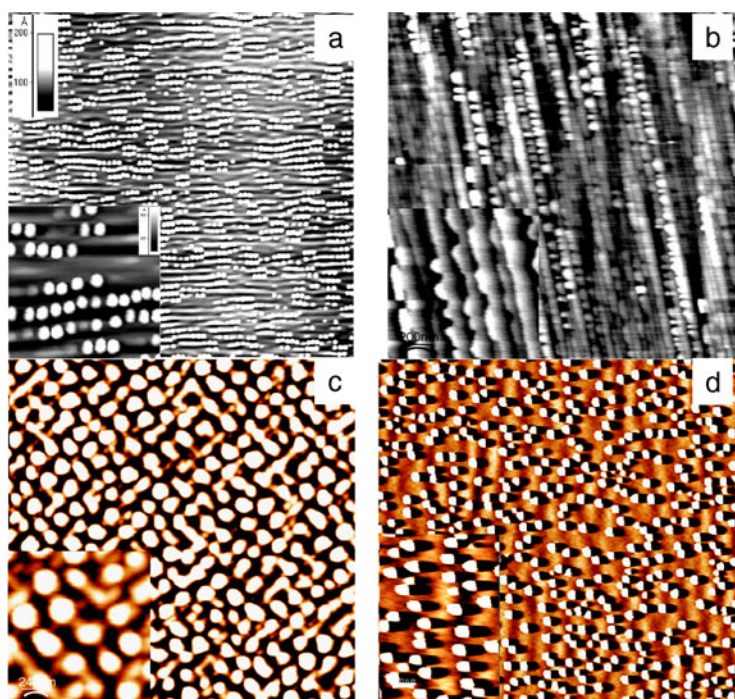
Figure 24. Self-organized Ge dots deposited on self-patterned substrates layers: (a) $Si_{0.75}Ge_{0.25}$ 10° off (001), (b) Si 2° off towards [11-2], (c) $Si_{0.75}Ge_{0.25}$ (001) and (d) Si 1.5° off (001).

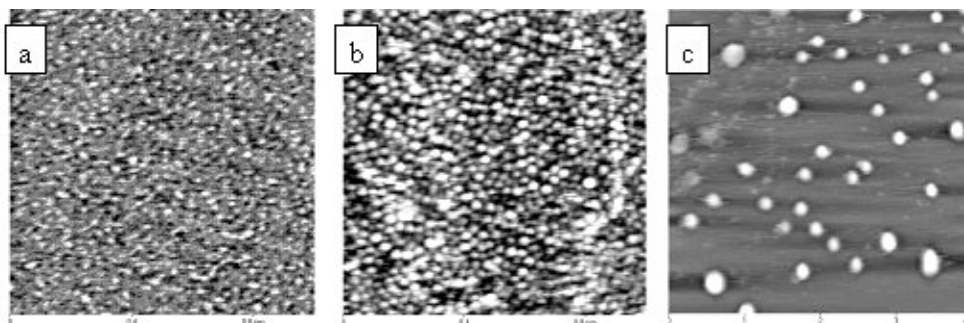**Figure 25.** AFM images after the growth of 18 Å of Ge on 1 ML Sb/Si(0 0 1): (a) $T_g = 350\,°C$, (b) $T_g = 550\,°C$, and (c) $T_g = 750\,°C$.

evidenced the partial desorption of Sb from the Si surface at 550 °C and not at 350 °C [83], this could modify the density of nucleation sites and be a possible way to modify growth.

In conclusion, for Sb-mediated growth of Ge/Si(001), we have demonstrated that the first effect of Sb is to promote the 2D growth and to delay the 2D–3D growth transition, probably due to the reduction of the surface energy. A second effect is that of inducing the formation of ultra-small islands (~30 nm) with high surface density (1.5×10^{11} cm^{-2}) and homogeneous surface distribution at higher temperature (550 °C). Moreover, Sb was found to decrease the adatom surface diffusion, and to change the equilibrium shape of islands. Sb-mediated growth was then found to be an interesting tool for realizing both very small Ge islands and smooth Ge surfaces.
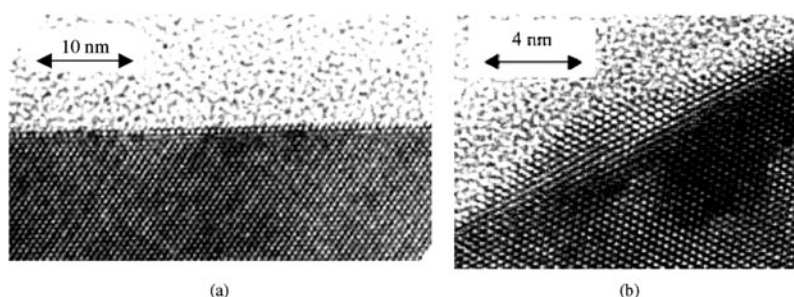
Figure 26. A cross-sectional TEM image of the 1 ML Sb-mediated growth of 1.8 nm of Ge at (a) $T_g = 350\,°C$ and (b) $T_g = 550\,°C$.

5. Redistribution of dopants

The fabrication of δ-doped Si/SiGe layers with controlled spatial distribution of the dopants normal to the growth plane is an important challenge because of the potential technological applications. The control of dopant distribution needs a complete understanding of diffusion, dynamic surface segregation, and desorption of the dopant atoms. We are concerned here with the incorporation/segregation of Sb and B during growth.

5.1. Segregation coefficient

SIMS profile analyses were performed to determine the segregation and incorporation coefficients for antimony (Sb) in Si or $Si_{1-x}Ge_x$ films as a function of temperature and Ge concentration in compressively stressed or relaxed samples [83]. The growth procedure producing Sb-doped layers buried below an undoped $Si_{1-x}Ge_x$ layer (see for instance the Sb depth profile of figure 27, upper part) consisted of temperature-programmed sequences, schematically represented in figure 27. After deposition of 0.44 ML of Sb at 400 °C, $Si_{1-x}Ge_x$ layers (with x varying between 0 and 0.2) were grown at constant temperature values Tg between 350 and 550 °C. At the end of this sequence, the sample was immediately cooled to ambient temperature (lower than 200°C) and covered by an amorphous Si layer (approximately 20 nm thick), intended to trap the surface-segregated dopant atoms.

Figure 28(a) shows the evolution of the Sb (SIMS) profiles in a pure Si layer grown at different temperatures (Tg). At LT (350 °C) two peaks can be observed: one (N_{seg}) relates to surface-segregated atoms and the other (N_{inc}) relates to incorporated atoms. As the growth temperature increases, N_{inc} vanishes at the expense of N_{seg}. The surface segregation coefficient (r_{seg}), which can be defined as the ratio of the integrated area of the surface peak (N_{seg}) to the total of pre-deposited impurity atoms ($r_{seg} = N_{seg}/N_{tot}$), varies exponentially versus the inverse growth temperature with $E_{activation} = 0.36$ eV (figure 28(b)). At 550 °C, the Sb sheet concentration ∼0.4 ML was determined by integrating the area of the peak. This value is in good agreement with the pre-deposited Sb coverage (∼0.44 ML). It confirms the negligible Sb desorption from Si(001) at this temperature.

A similar set of experiments have been performed for the growth of biaxially strained $Si_{1-x}Ge_x$ films on Sb/Si(001). A first interesting feature concerns the thermal desorption of Sb atoms from $Si_{0.9}Ge_{0.1}$ and $Si_{0.8}Ge_{0.2}$ surfaces, which occurs at 550 °C, in contrast to the negligible desorption observed from the Si surface. Similar results have been found by Falkenberg *et al* [88]. This phenomenon can be attributed to the lower heat of sublimation of Ge leading to lower Sb–Ge bond breaking energy in comparison to that for Sb–Si. In addition,
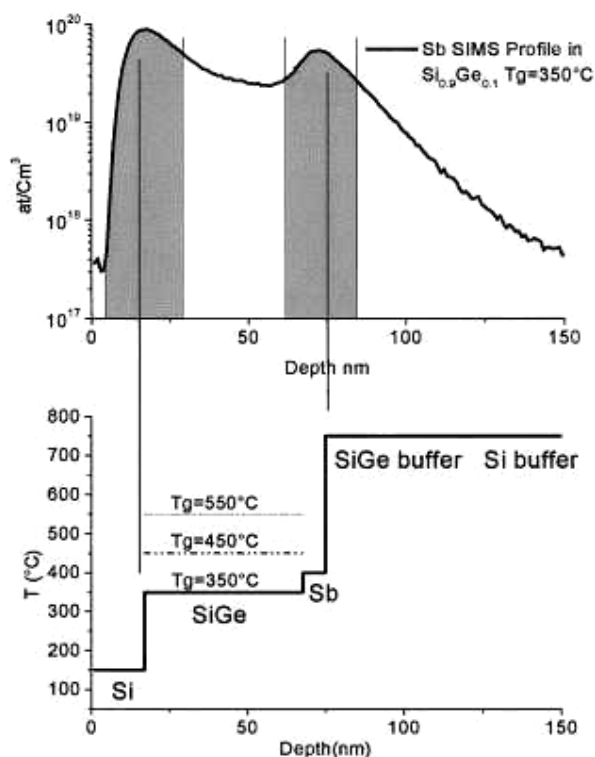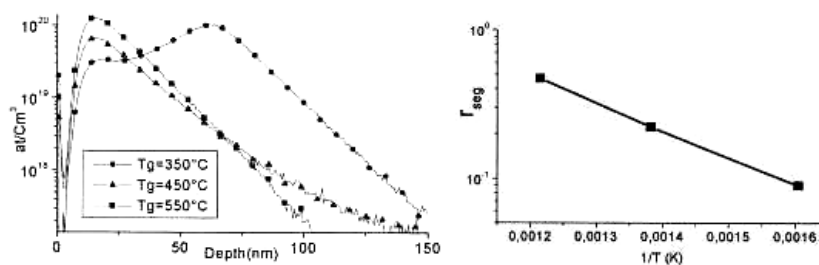
Figure 27. Temperature sequences during growth.

Figure 28. (a) SIMS profiles of Sb in Si: $Tg = 350, 450$ and $550\,°C$. (b) The Sb surface segregation coefficient (r_{seg}) measured in Si.

calculations [89] have shown that each Sb–Si bond is approximately 0.1 eV stronger than each Sb–Ge bond. For details on Sb thermo-desorption phenomena, see [90].

From SIMS profiles, we also measured the incorporation coefficient (r_{inc}), which is determined as the ratio of the integrated area of the peak (N_{inc}) to the total of pre-deposited impurity atoms. The Ge composition dependences of r_{inc} and r_{seg} are presented in figure 29. A surprising feature is that Sb-atom segregation increases with increasing Ge concentration in strained samples. Similar results have been reported by Fujita *et al* [91], in contrast to the results obtained for B atoms that are preferably incorporated in $Si_{1-x}Ge_x$ layers [92, 93].

The driving force for Sb segregation is still a matter of debate since contradictory results have been obtained (both experimentally and theoretically). Discrepancies between Sb and
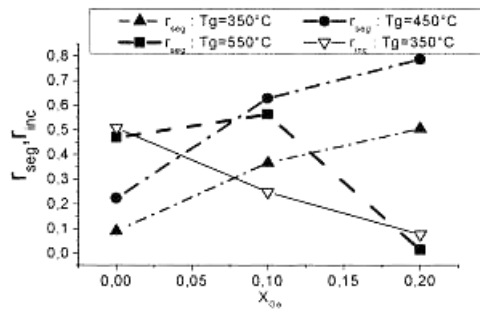
Figure 29. Coefficients of Sb surface segregation (r_{seg}) and incorporation (r_{inc}) in $Si_{1-x}Ge_x$.

B dopant-atom segregation/incorporation were mainly attributed to their different atomic sizes [93]. As regards the B behaviour, it was established that the reduced B surface segregation in $Si_{1-x}Ge_x$ films is due to the partial compensation by Ge atoms with larger atomic sizes of the tensile strain induced by the smaller size of B atoms. Another explanation based on differences between the bond breaking energies of B–Si, Si–Si, and Sb–Si has been given by Ushio *et al* [94] from density functional calculations (without taking into account the strain). The lowering of the barrier energy at the numerous step edges induced by Sb during growth is also invoked [95–97].

In order to model Sb surface segregation during the growth of Si and $Si_{1-x}Ge_x$ layers during MBE experiments, calculations using a two-state atomic exchange model were performed and will be detailed elsewhere. Briefly, segregation is mainly driven by two contributions: an activation barrier for dopant-atom motion and an energetic term including chemical (alloying) and size effects and surface free energy. In such a model, the energetic contribution is not favourable at an increased surface segregation with increasing Ge ratios in $Si_{1-x}Ge_x$. In addition, by fitting the experimental results, we found that the kinetic activation barrier predominantly controls the evolution of Sb segregation in the overall range of temperature. We suggest that a lower kinetic barrier for Sb-atom motion in $Si_{1-x}Ge_x$ can be invoked to explain this behaviour.

In order to separate the chemical (Ge concentration) and the strain (induced by the epitaxy) effects, five samples consisting of epitaxied $Si_{1-x}Ge_x$ structures were grown: three fully strained with Ge contents $x = 0$, 0.09, 0.18 and two relaxed with $x = 0.09$, 0.18. The Ge composition of the layers was checked using Rutherford backscattering spectrometry (RBS). The structure of samples is a stacking of five layers (four for the relaxed sample) consisting of:

(a) 50 nm of $Si_{1-x}Ge_x$ deposited at 650 °C;
(b) one monolayer of Sb ($\sim 3 \times 10^{14}$ at cm^{-2}) deposited at 400 °C (this Sb quantity will be referred to as Q_t in the following);
(c) 6 nm of $Si_{1-x}Ge_x$ deposited at 200 °C;
(d) 45 nm of $Si_{1-x}Ge_x$ deposited at 550 °C;
(e) a 20 nm Si cap deposited at $T < 200$ °C only on strained structures.

Layer (c) was grown at an unusually low temperature (200 °C) in order to bury as much as possible of the Sb, to obtain δ-doping, which can be used as a diffusion source. However, even at this very low growth temperature, part of Q_t should segregate to the surface. In order to restore the crystallographic quality of this layer, a 5 min anneal was performed at 750 °C before deposition of layer (d). This annealing temperature was decreased to 600 °C for the
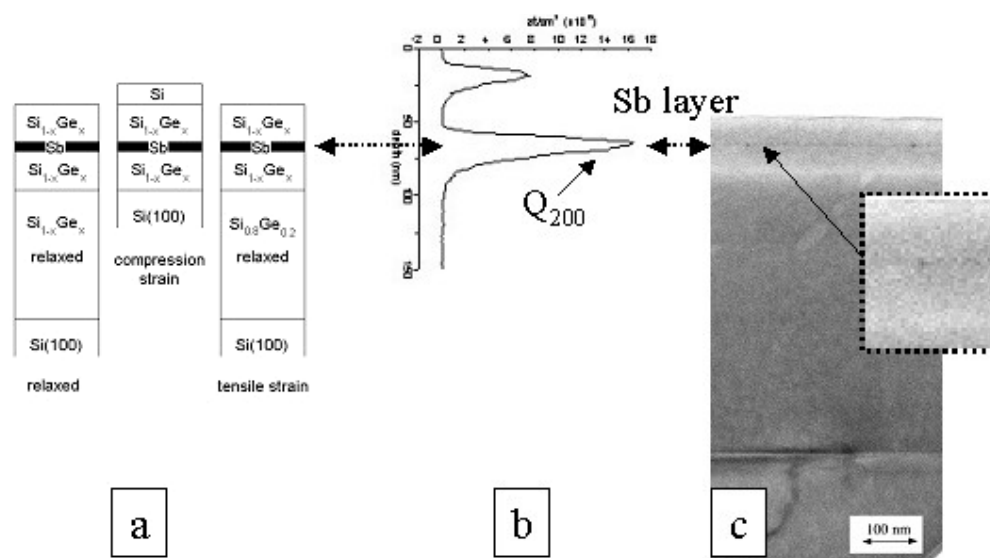
Figure 30. (a) samples structures, (b) Sb concentration profile obtained by SIMS for a $Si_{0.82}Ge_{0.18}$ layer epitaxially grown on Si(001) and (d) TEM cross section view of a Sb δ-doped $Si_{0.91}Ge_{0.09}$ layer tensely strained on a relaxed $Si_{0.81}Ge_{0.19}$ pseudo-substrate grown on Si(001)..

relaxed sample to limit dislocation propagation in the topmost layer. Sb concentration versus depth profiles were measured by SIMS using a Cameca IMS4F operated at 8 keV with O_2^+ primary ions. Figure 30 shows a typical Sb concentration versus depth profile obtained for the $Si_{0.82}Ge_{0.18}$ biaxially compressed sample. Two spikes are observed, the surface spike resulting from the Sb segregation during growth at 550 °C (layer (d)), and a spike observed at about 50 nm (Q_{200}) corresponding to the Sb incorporated during the growth of layer (c) at 200 °C.

The Sb incorporation coefficient at 200 °C is defined as the ratio between the integration of the peak Q_{200} and the total amount of Sb deposited, Q_t. Figure 31 presents the evolution of this coefficient versus the Ge composition (x) in the compressed and relaxed layers. Since the surface segregation shows the opposite behaviour to the incorporation (there is no Sb desorption at 200 °C), one can conclude that the Sb segregation during growth decreases in relaxed layers and increases in biaxially compressed layers when x increases. One can note that the Sb incorporation in relaxed Si_xGe_{1-x} layers is close to 1 whatever the Ge concentration ($x = 0.09$ and 0.18).

These variations of Sb surface segregation with Ge concentration and strain may originate from a modification of:

 (i) the equilibrium segregation energy E (the driving force of the process);
(ii) the rate of exchange between the Sb-segregated sublayer and its immediate neighbours (the kinetics of the process).

equilibrium segregation of Sb in Si has three main components which, in order of decreasing importance, are

  (i) a lower Sb surface energy (γ),
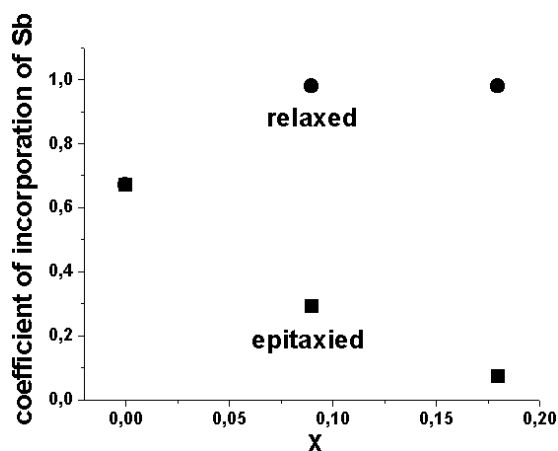 (ii) a larger Sb atomic size (r),
(iii) a strong tendency to phase separation.

Figure 31. Sb incorporated during the growth at 200 °C of relaxed (●) and epitaxially grown (■) $Si_{1-x}Ge_x$ layers versus the Ge composition (x).

If Ge is added to Si, one expects:

  (i) a decrease of the surface energy of the Si(Ge) alloy (Ge has a lower surface energy than Si and segregates on Si) and,

 (ii) an increase in the alloy lattice parameter.

Both effects should induce a decrease in Sb equilibrium segregation. Moreover, since Sb–Ge interactions are also repulsive, there should not be any synergetic influence between Ge and Sb surface segregation.

Considering compressive stress, since Sb has a larger size than Si (or Ge), the segregation of Sb should be slightly larger in strained than in relaxed structures. However, if one considers that the main driving force for surface segregation is the minimization of surface energy, one can expect the equilibrium segregation of Sb to decrease both in relaxed and in epitaxially strained $Si_{1-x}Ge_x$ layers when x increases (even if this decrease is less important in strained layers).

The opposite variations (increase for strained layers, decrease for relaxed layers) which are observed for Sb segregation during MBE growth are thus difficult to understand if one takes into account only equilibrium driving forces. The origin of this behaviour is more likely to be found in the kinetics of the process, as is the case for the variations with temperature.

In order to evaluate kinetic parameters, we measured in the same layers the Sb lattice diffusion coefficient as a function of strain and Ge composition. These measurements are based on the analysis of the modifications of the incorporated Sb distribution induced by an additional heat treatment. The variations of the Sb diffusion coefficients with Ge composition in relaxed and compressively strained layers are presented in figure 32 for a temperature of 800 °C. One can observe that Sb diffusion coefficients increase in relaxed and strained layers, the increase being larger in strained layers. This behaviour can be explained by the mechanism of diffusion of Sb in $Si_{1-x}Ge_x$ which is vacancy mediated. The activation barrier of diffusion decreases with Ge concentration (chemical effect) and, at constant Ge concentration, with biaxial compression (stress effect). In epitaxial layers, the increase of the Sb diffusion coefficient is thus linked to the addition of the two effects. Even if one cannot use directly the volume diffusion coefficients for the kinetics of the exchange between the free surface and its
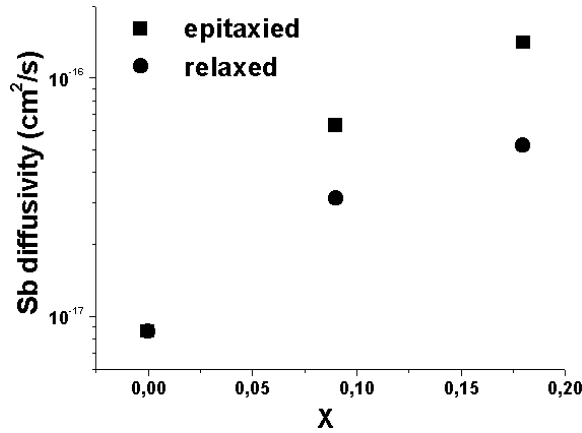
Figure 32. Variation of the coefficient of diffusion of Sb at 800 °C in relaxed (●) and epitaxially grown (■) $Si_{1-x}Ge_x$ layers versus the Ge composition (x).

immediate neighbours, one can expect the tendencies observed for lattice diffusion coefficients to be maintained, which would mean that the activation barrier for diffusion scales as

$$Q_{dif}(\text{Si}) > Q_{dif}(\text{Si}_{1-x}\text{Ge}_x)_{relax} > Q_{dif}(\text{Si}_{1-x}\text{Ge}_x)_{strained}.$$

while the former discussion on equilibrium segregation suggests that

$$-E_{seg}(\text{Si}) > -E_{seg}(\text{Si}_{1-x}\text{Ge}_x)_{strained} > -E_{seg}(\text{Si}_{1-x}\text{Ge}_x)_{relax}.$$

Using these modifications of E_{seg} and Q_{dif} in the framework of a two-state exchange model taking into account both the driving force for segregation (E) and the kinetics of the process (Q), it is possible to show that the Sb surface segregation during growth follows different kinetic regimes in relaxed and compressed layers. In the case of relaxed layers the evolution is more probably dominated by the modification of the segregation enthalpy, while in compressed layers the larger decrease of the Sb diffusion barrier promotes Sb segregation.

5.2. Doping control

We are concerned here with the incorporation of boron during GSMBE, for which two different approaches are feasible. In the first, which is the most used so far, B is supplied simultaneously with Si and Ge and is incorporated directly in the growing Si or $Si_{1-x}Ge_x$ film. It is generally shown that the dopant incorporation is a non-equilibrium process which is mainly dependent on the experimental kinetic parameters (temperature, flux ratios, growth rates and time, etc). The alternative procedure is to pre-deposit an ordered sub-monolayer quantity of B on which epitaxial layers of Si or $Si_{1-x}Ge_x$ are subsequently grown. Despite many comprehensive studies of the B doping of Si, very little is known about the application of this technique and its comparison with direct deposition. We briefly present here the results of a comparative study in which we are able to demonstrate an enhanced incorporation rate and a decrease in the concentration decay length with B pre-deposition. The technique has limitations however, which are related to the equilibrium steady-state coverage as a 2D film. Beyond this coverage, surface roughening due to 3D island growth occurs, which is detrimental to the Si or crystalline quality. In order to achieve sharp doping profiles we used different procedures and we showed that the combination of pre-deposition and co-deposition is the most efficient method for achieving highly doped layers (up to 7×10^{19} cm^{-3} in Si and up to 2×10^{19} cm^{-3} in $Si_{1-x}Ge_x$). For a detailed analysis of B incorporation in Si and $Si_{1-x}Ge_x$ films, see [92].

B_2H_6 is known to adsorb dissociatively on Si(001) over the typical range of temperatures used in Si growth from disilane (500–1000 °C). The saturation coverage is reduced by the presence of surface hydrogen, so higher B coverages are expected to occur at higher deposition temperatures ($Great$ 600 °C), where hydrogen desorbs from the Si surface [98]. In ultrahigh-vacuum chemical vapour deposition (UHVCVD), for temperatures around 600 °C, the sticking probability of B_2H_6 during adsorption was reported to be $<10^{-4}$ [99] while for co-deposition of B and Si (simultaneous supply of B_2H_6 and Si_2H_6) published values range from 6.4×10^{-4} at 600 °C to 1.4×10^3 at 950 °C [100], even though gas interaction considerations would predict a lower sticking probability in the latter case. The equilibrium solubility limit of electrically active B impurity in Si increases from 7×10^{18} atoms cm^{-3} at 500 °C to 3×10^{19} atoms cm^{-3} at 700 °C [101] but values one decade higher have been reported in films prepared by CVD and attributed to the non-equilibrium nature of the process [102]. B diffuses substitutionally in Si (by jumping from one vacant lattice site to the next), so to restrict diffusion and maintain sharp interfaces, low deposition temperatures (or high growth rates) are needed. Bulk diffusion of B in Si has been described [103] in the case of co-deposition of B_2H_6 and Si_2H_6 and in the case of a pre-deposited surface source. The calculated decay lengths for the two different processes are in the same range (see [92]). The deposition time was assumed to be 10 min, which represents a minimum value for any relevant device structures. Experimentally, this implies that above 700 °C we would not achieve realistic δ-doping due to the large decay length ($\sim$4 nm) of the doped layer and to the formation of disilicides [104]. Conversely, it has been reported that B diffusion is totally suppressed below $\sim$500 °C [105, 106]. Bulk diffusion is not, however, the only process responsible for mass transport of B in Si. Motion in the growth direction (usually called 'segregation') is driven by other mechanisms which cannot be described as bulk diffusion. This results in both smearing of the dopant profiles and an enrichment of B at the surface with respect to the bulk concentration, as demonstrated in many experimental studies (e.g. [107–109]). The origins invoked for the segregation are principally the reduction of the strain at the surface (surface reconstruction, for example [110]) and the reduction of the surface free energy. Several atomistic models have been proposed to describe the process [111–114]. The results for As segregation during Si growth by GSMBE and also for Ge segregation in $Si_{1-x}Ge_x$ have been explained by the two-site exchange model [115–118]. This considers that segregation occurs only by atomic interchange between a sub-surface layer and a growing (Si) surface layer. The process can occur either in a kinetically controlled regime (where segregation is slow relative to the growth rate) or in an equilibrium regime (where segregation is fast relative to the growth rate). Although the model is empirical, the rate equations involved allow the Gibbs energy of segregation and the segregation barrier to be determined from measurements of dopant profiles.

However, in the present case of B in Si we were unable to determine accurately the doping profile at various temperatures because of experimental difficulties:

(i) measurement of the low-B-coverage surface layer;
(ii) the mixing of diffusion and segregation mechanisms at temperatures in the range 650–700 °C;
(iii) the realization of experiments with constant growth rates over a wide temperature range (from 500 to 700 °C).

In GSMBE experiments (low growth rates), optimal B doping conditions result from a compromise between temperature and growth rate, which are interdependent. Finally, creating an atomically flat surface is a matter of serious concern in devices with Si/Ge-doped heterostructures. Since these devices utilize the band discontinuity at Si/Ge interfaces, the flatness of the layers is very important for obtaining high-quality device performances.
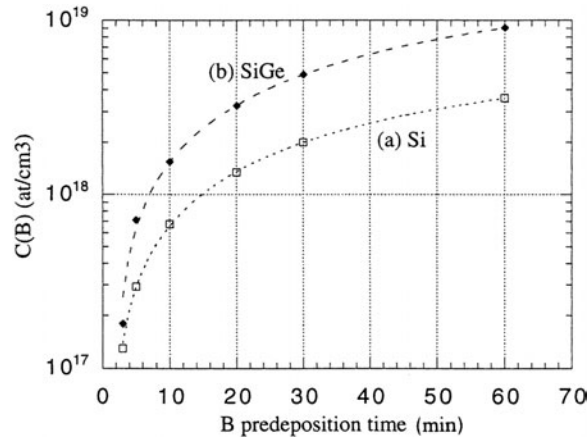
Figure 33. Evolution of $C(\text{B})$ with the pre-deposition time in (a) Si layers ($\square$) and (b) SiGe layers ($\blacklozenge$).

However, even though one study reported flat (B-) doped layers with perfect crystallinity for B concentrations $\sim 10^{20}$ cm^{-3} [102], it is generally assumed that B-induced roughening occurs in the doping level range 10^{17}–10^{20} cm^{-3} and becomes disastrous above $\sim 10^{20}$ cm^{-3} [92, 119, 120]. In particular, high-resolution transmission electron microscopy (HRTEM) observations reveal microprecipitates and extended defects throughout the films in addition to enhanced surface roughening, caused by the appearance of {113} facets [121]. Scanning tunnelling microscopy (STM) studies have explained the B-induced surface roughening by the pinning of the Si dimer rows leading to an enhanced roughness of the S_B step edges (perpendicular to the dimer rows [122]), at B coverage as low as 0.06–0.08 ML [105]. By contrast, Si$_{1-x}$Ge$_x$ layer morphology and crystallinity are expected to be improved in highly doped samples, since substitutional boron induces partial strain compensation because of its smaller atomic radius [123]. Increases of both the critical thickness [124] and of the B incorporation level [125] have been demonstrated for heavily boron-doped Si$_{1-x}$Ge$_x$ layers.

We are concerned here with the two competing processes of (i) incorporation and (ii) segregation occurring during B doping. The incorporation levels are investigated in the first part by measuring the SIMS and $eC(V)$ concentration profiles. We distinguish in this part the two-dimensional sheet concentration of B ($N_{2D}(\text{B})$) determined by measuring the total integrated intensity under a B peak of the SIMS profiles and the highest B concentration spike ($C(B)$) directly extracted from the data (see [92]). Because of the well-known surface-roughness-induced artefacts in the SIMS depth profiling technique [126], we decided to report only on those samples having perfect crystallinity and low surface roughness.

In this set of experiments, the quantity of B incorporated in the Si or Si$_{1-x}$Ge$_x$ overlayers only comes from the pre-deposition step. Since no desorption of B is expected to occur below 900 °C, $N_{2D}(\text{B})$ also represents the B surface coverage obtained during that pre-deposition step. B pre-deposition was performed between 450 and 600 °C. The sticking coefficient was found to be about 3×10^{-3} and nearly independent of temperature. Figure 33 represents the evolution of $C(\text{B})$ with the pre-deposition time. After one hour of B deposition (which corresponds to ~ 12 L exposure, i.e. 12×10^{-6} Torr s) both $N_{2D}(\text{B})$ and $C(\text{B})$ slowly saturate. Under these conditions (B$_2$H$_6$ partial pressure $\sim 7 \times 10^{-9}$ Torr), maximum values of $N_{2D}(\text{B}) \sim 2 \times 10^{13}$ atoms cm^{-2} and $C(\text{B}) \sim 4 \times 10^{18}$ atoms cm^{-3} were achieved. Figure 34 shows the evolution of $N_{2D}(\text{B})$ with the B flux, in the pressure limits of the GSMBE chamber (partial pressure
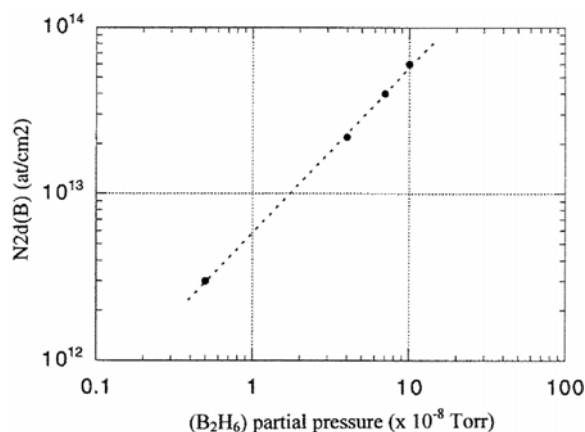
Figure 34. Evolution of the total sheet density in boron-doped Si with the partial pressure of B_2H_6 in the chamber during the pre-deposition.
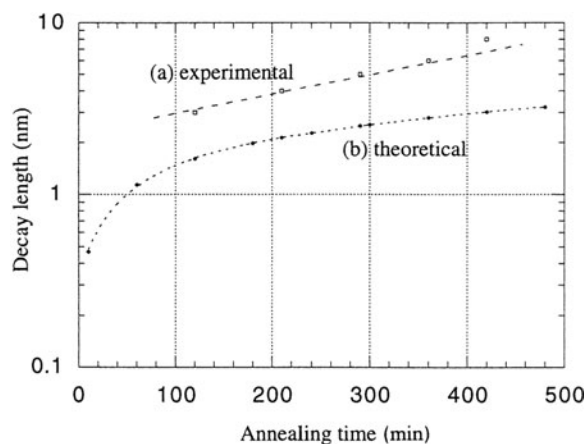

Figure 35. Theoretical decay length as a function of the annealing time compared to the experimental data.

between $\sim 7 \times 10^{-9}$ and 1.3×10^{-7} Torr). In fact, 1/10 ML coverage is obtained for ~ 30 L exposure and there is no further increase. B pre-deposition on $Si_{1-x}Ge_x(001)$ with $x = 0.1$ was performed under the same experimental conditions. The sticking coefficient extracted from these data ($\sim 10^{-3}$) is lower than on Si. This lower sticking coefficient has not been explained so far, but it could be related to a higher Ge–B bond energy.

Furthermore, we observed a higher $C(B)$ for $Si_{1-x}Ge_x$ alloys than for Si without degradation of the surface morphology. Even though accurate values are difficult to determine due to the broadening effect of the SIMS profiling technique, the diffusion length (L_{diff}) is to a first approximation in good agreement with the calculated ones [108] (figure 35), confirming the substitutional diffusion of B into bulk Si. A smaller L_{diff} of B in $Si_{1-x}Ge_x$ than in Si is obtained, probably due to the larger size of Ge atoms reducing the mobility of B in the crystalline lattice. In all cases, below 600 °C, L_{diff} is below the SIMS broadening limit and cannot be measured. Examples of sharp δ-doped Si layer SIMS profiles are presented in figure 36. They were obtained for a B exposure of 63 L (B_2H_6 partial pressure $\sim 1.3 \times 10^{-7}$ T) and an Si growth
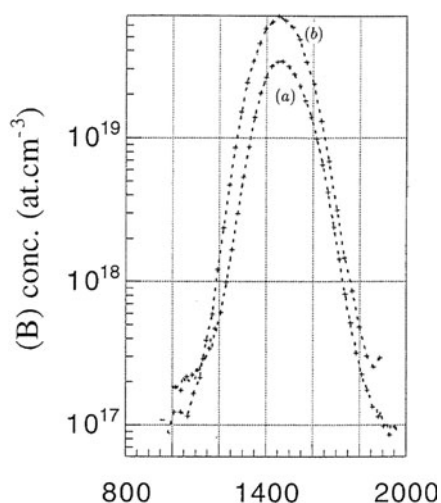
Figure 36. Comparison between the SIMS profiles of two Si boron δ-doped layers. The pre-deposition was performed with 63 L of B_2H_6 and an Si overgrowth of (a) 520 °C and (b) 600 °C. A higher incorporation of boron is obtained at 600 °C.

temperature of (a) 520 °C and (b) 600 °C. For a similar decay length ($\sim$8 nm/decade), a slightly higher incorporation level is obtained for Si growth at 600 °C. In that case, confirmation of the sharp decay length is given by $eC(V)$ profiling (figure 37). Similar experiments were performed for $Si_{0.8}Ge_{0.2}$ layers and boron deposition at (a) 550 °C and (b) 600 °C. The SIMS results are presented in figure 38. We obtained narrower peaks than for Si, with decay lengths inside the SIMS detection limit. Again, the higher the pre-deposition temperature, the higher the boron incorporation.

In order to achieve sharp δ-doping layers with $C(B)$ in the 10^{20} atoms cm^{-3} region (which corresponds to a B concentration of $\sim$0.2% in the Si layer) we used flux ratios ($J_{B_2H_6}/J_{Si_2H_6}$) between 4×10^{-4} and 8×10^{-3}. The variation of the incorporated B concentration $C(B)$ as a function of $J_{B_2H_6}$ is determined from the $eC(V)$ profiles. Figure 39 shows that $C(B)$ increases linearly with $J_{B_2H_6}$. In comparison with the previous experiments, similar decay lengths were obtained but the maximum $C(B)$ which could be achieved ($C(B) \sim 10^{19}$ atoms cm^{-3}) was much lower. The δ-doped layers with the sharpest profiles were in fact obtained (for both Si and $Si_{1-x}Ge_x$) by combining pre-deposition of B with a short B deposition during Si (figure 40) or $Si_{1-x}Ge_x$ (figure 41) growth.

We will now consider the segregation effect. The measured segregation length (L_{seg}) is nearly independent of the pre-deposition time, i.e. of the boron surface coverage, which means that for our experimental conditions the growth rate is always lower than the segregation rate. Consequently, an equilibrium state, detailed in the next section, is reached before the end of the growth experiment. Qualitatively, L_{seg} increases with the growth temperature, but the evolution is difficult to determine quantitatively. In all cases a smaller L_{seg} is found in $Si_{1-x}Ge_x$ alloys than in Si (figures 36 and 38), which is attributed to the competitive segregation of Ge and of B. This effect has been employed to incorporate two types of dopant in Si in order to limit the segregation length of one of them. In order to quantify the B segregation and to control its influence on the Si or $Si_{1-x}Ge_x$ growth mechanisms, we have recorded and analysed the RHEED oscillations:

(i) before and after B pre-deposition and
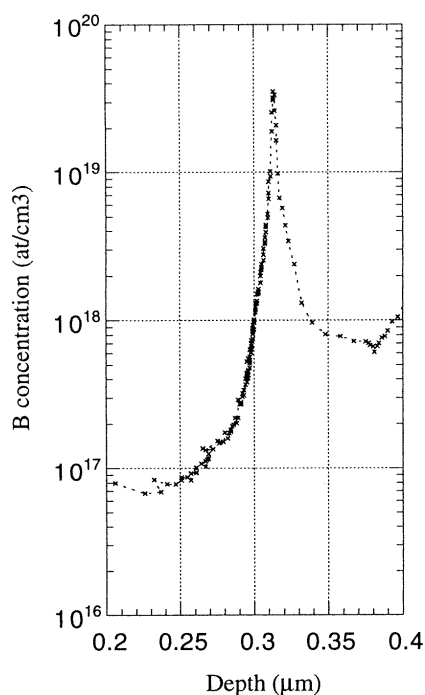(ii) during co-deposition of B and Si at various B/Si flux ratios.

Figure 37. Hole density measured by $eC(V)$ profiling of the Si boron δ-doped layer grown at 600 °C confirming the SIMS profile presented in figure 36(*b*).

Throughout the experiments, the RHEED reconstruction remains $(2 \times 1) + (1 \times 2)$ during the complete deposition of B and also during the growth of Si.

First, the growth rate of Si (R_{Si}) was reduced by 20% whatever the quantity of B pre-adsorbed on the Si surface (figure 42). In addition, once B was adsorbed on the surface, R_{Si} never completely recovered its previous value (for pure Si/Si) and remained slightly lower even after Si deposition at 750 °C for some hours. Experiments performed during co-deposition of Si and B produced identical decreases of R_{Si} whatever the $J_{Si_2H_6}/J_{B_2H_6}$ ratio used (between 4×10^{-4} and 8×10^{-3}). Moreover, the damping coefficient of the oscillations was not affected by the B pre-adsorption, even at the critical temperature of transition from 2D nucleation to step flow growth (figure 43). This result proves that the surface diffusion of Si adatoms is not modified by the presence of B and the preferential adsorption of B on step edges cannot therefore be invoked to explain the B-induced decrease of R_{Si}. Identical behaviour was also observed for the growth of SiGe alloys. Over the range of temperatures studied and for various B_2H_6 pre-deposition pressures, the growth rate of the SiGe overgrown layer is reduced by $\sim$15%. However, the growth rate recovered more rapidly to its previous value (for pure SiGe/Si) after the growth of a thick buffer layer of Si. Very few previous studies have considered the influence of B doping on the Si growth rate, but it is commonly assumed that it is not affected by low concentrations of B. Glass *et al* [127] reported that B doping concentrations of $>6 \times 10^{19}$ atoms cm^{-3} increase R_{Si} by up to 50% at LT but reduce it by the same amount at HT.

At LT the R_{Si}-increase was attributed to a weakening of the Si*–H bonds favouring H desorption, while at HT the R_{Si} decrease was attributed to the deactivation of a fraction of the Si dangling bonds. We have clearly shown that over a large range of B doping concentrations
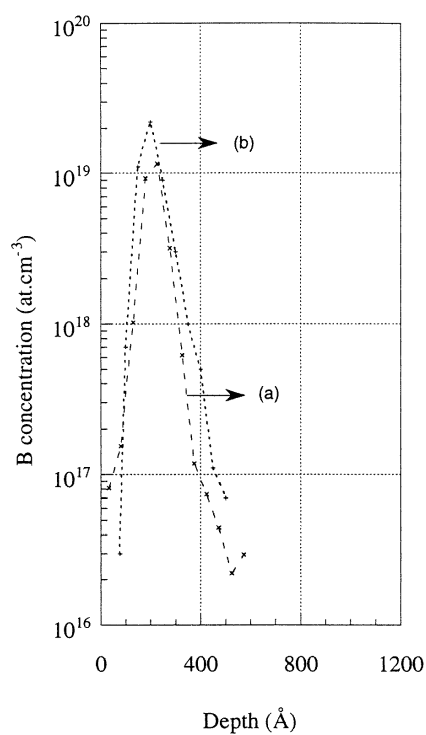
Figure 38. Experiments similar to those of figure 36, but on $Si_{0.8}Ge_{0.2}$ layers with overgrowth at (a) 550 °C and (b) 600 °C. Narrower peaks are obtained than for Si but the same trend is observed.
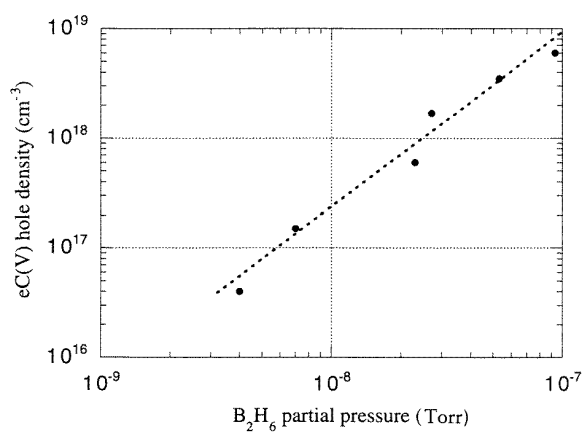

Figure 39. Hole density measured by $eC(V)$ profiling. The hole density increases linearly with the B_2H_6 pre-deposition time.

the small decrease of R_{Si} observed is not related to the quantity of B incorporated in the layer. Now if we consider (in agreement with the results reported above) that the R_{Si}-decrease is related to deactivated dangling bonds, this means that in our experiments the quantity of B at the free surface is the same for very different quantities of B incorporated, which demonstrates conclusively that the quantity of B in the surface layer reaches saturation (equilibrium) coverage
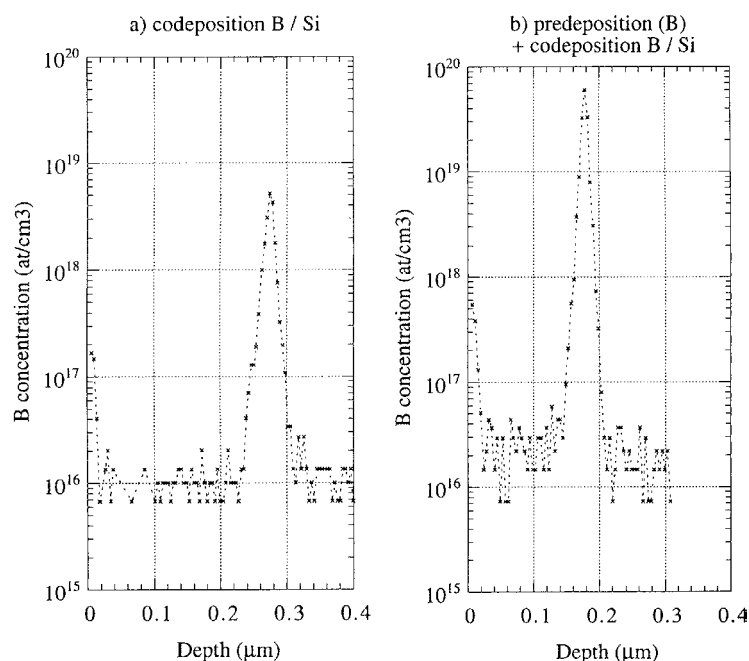
Figure 40. Comparison between the SIMS profiles of (a) a co-deposition of B_2H_6 and Si_2H_6 followed by Si deposition and (b) a pre-deposition of B_2H_6 followed by a short co-deposition of B_2H_6 and Si_2H_6. The decay lengths obtained are similar, but a higher doping is reached with the co-deposition step.

that minimizes the surface free energy, as occurs for many doping species (Sb, As, and Ga for instance). We assume that in the experiments presented here, the critical equilibrium coverage is reached over the complete range of exposures tested. In accordance with the atomic model of Zhang *et al* [111], which indicates that high local stresses are induced by Si–B bonds, it can easily be assumed that for coverages higher than the equilibrium limit, B agglomerates into 3D islands in order to reduce the surface free energy (this is also the case for the doping species cited above). 3D islands would explain the different coverage levels obtained for the different exposures during B pre-adsorption. The coverage would then be limited by the shape of the B clusters, which become highly metastable for large heights and low lateral sizes.

Finally, a constant fraction of B continues to segregate at the growing surface during Si overgrowth. This 'floating' submonolayer of B maintains the critical equilibrium coverage and deactivates a fraction of the dangling bonds. This explains why in all our experimental conditions a constant reduction of R_{Si} is observed, even after the growth of thick Si buffer layers. Since the analyses reported in this work cannot give any information on the quantity of B floating at the surface (due to the abrasion process used), further analyses are needed to determine this quantity and to confirm the mechanism proposed.

In summary, it was shown that the combination of pre-deposition and co-deposition is the most efficient method for achieving highly doped layers (up to 7×10^{19} cm^{-3} in Si) with very abrupt interfaces and low surface roughness. The necessity of a brief co-deposition step was explained by there being a limit to the coverage of boron before islanding occurs during the pre-deposition step, which limits the maximum incorporation of boron and degrades the film morphology. The best results were obtained with boron doping at 600 °C. Lower doping
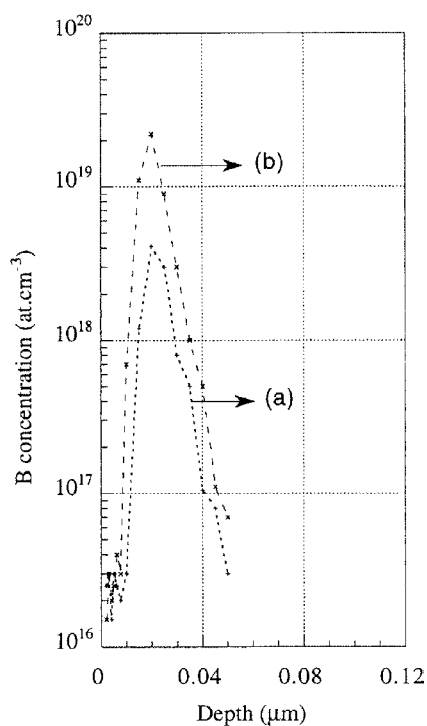
Figure 41. Experiments similar to those of figure 12 but on $Si_{0.8}Ge_{0.2}$ layers. The decay lengths are very small in both cases (below the SIMS resolution limit) but a higher doping is reached for the two-step deposition process.
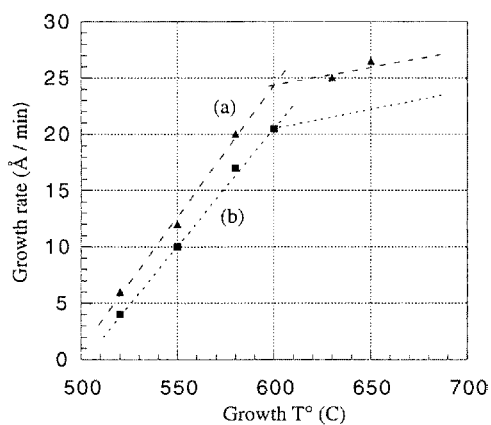

Figure 42. The growth rate of Si (a) compared to the growth rate of Si after a pre-deposition of boron (b). Over the range of temperatures studied and for various B_2H_6 pre-deposition pressures the growth rate of the Si overgrown layer is reduced by 20%. Similar results are obtained during co-deposition of B_2H_6 and Si_2H_6 with various ratios of $J_{B_2H_6}/J_{Si_2H_6}$

levels were obtained in SiGe but with sharper interfaces than in Si. Supported by a RHEED oscillation study, we propose that there is a very stable surface coverage 'floating' during the subsequent overgrowth of both Si and SiGe, to explain the observed decrease of the growth rate and the previous results.
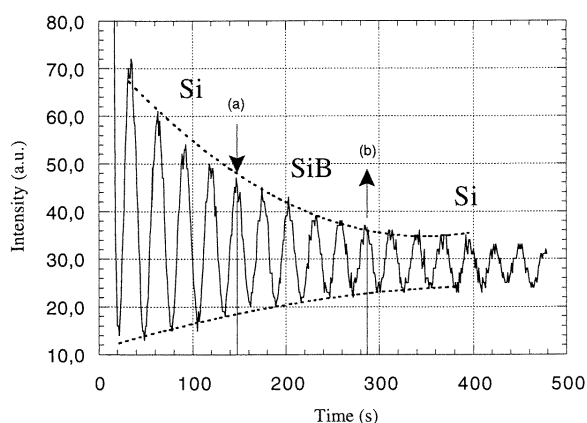
Figure 43. RHEED oscillations before, during, and after co-deposition of boron ($J_{B_2H_6}/J_{Si_2H_6} = 8 \times 10^{-3}$) in Si. No noticeable change in the damping of the oscillations with time is observed. Growth was performed at $\sim$600 °C which corresponds to the transition between 2D nucleation and step flow growth modes. This explains the high damping coefficient of the oscillations.

6. Physical properties

Beyond the understanding of growth mechanisms, the ultimate aim in building self-organized $Si_{1-x}Ge_x$-based nanostructures is to produce compounds showing good optoelectronic qualities. As a consequence, the testing of electronic properties of as-grown material is an appropriate way to assess $Si_{1-x}Ge_x$ structures. Electronic characteristics of heterostructures have been widely tested by luminescence techniques (PL, electroluminescence (EL), cathodoluminescence (CL)) and by electrical means mainly based on a capacitance–voltage (C–V) methodology.

PL experiments have been carried out on various $Si_{1-x}Ge_x$ heterostructures showing a wide range of growth conditions (growth technique, growth temperature, Ge content, nominal $Si_{1-x}Ge_x$ layer thickness, substrate orientation, template heterostructures, . . .).

Complete optical and electrical studies on fully strained [128] and relaxed [129] $Si_{1-x}Ge_x$ 2D wells grown by the chemical vapour deposition (CVD) technique have been reported.

Rapid thermal CVD-grown (RTCVD-grown) strained double heterostructures (DH) (with a Si cap covering the SiGe layer) and single heterostructures (SH) (without any Si cap on the $Si_{1-x}Ge_x$ layer), grown at 800 °C with Ge contents ranging from 7 to 19%, were studied [99]. In this work free excitonic recombinations were clearly characterized in all capped structures (DH) whereas they were absent in uncapped layers (SH). As free excitons are mainly localized in the $Si_{1-x}Ge_x$ layer due to the band line-up; this result clearly shows that the Si capping layer completely annihilates the high $Si_{1-x}Ge_x$ surface recombination velocity and consequently increases the radiative recombination rate.

It has also been shown that PL line characteristics can be used to extract structural properties of the $Si_{1-x}Ge_x$ alloy. For instance the ratio I_{NP}/I_{TO} (intensity of the non-phonon (NP) line over the intensity of the phonon-assisted transverse optical (TO) replica) has been used to study alloy disorder in the $Si_{1-x}Ge_x$ layer. This ratio showed a good matching with the probability of finding a Si–Ge pair, i.e. followed a $x_{Ge}(1 - x_{Ge})$ curve [129]. In addition the NP line FWHM has be used to control layer relaxation and interface roughness.

As we discussed in the previous sections, the $Si_{1-x}Ge_x$ growth mode can lead to the formation of dislocation-free 3D islands showing a large distribution of size and morphology depending on growth conditions, level of stress, etc. In order to assess the capabilities of those
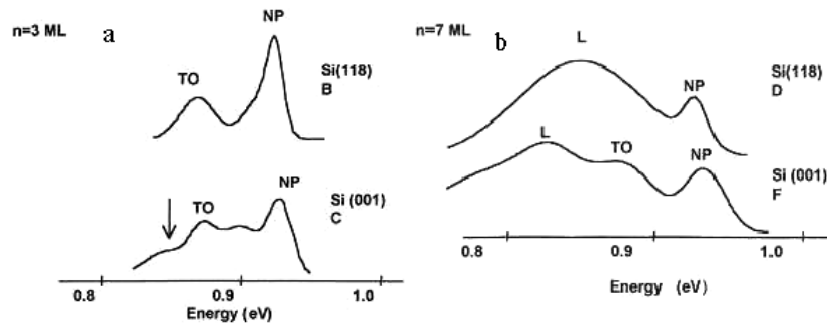
Figure 44. PL spectra of Si/nGe/Si$_{0.7}$Ge$_{0.3}$/Si structures obtained at 6 K on (001) and (118): (a) $n = 3$ ML, (b) $n = 7$ ML.

Ge-rich crystalline clusters as trapping dots for excitons, several PL studies on encapsulated Si$_{1-x}$Ge$_x$ nanostructures have been carried out [130, 131].

In [5] a strong relation between morphology and luminescence of islands grown on template layers (nGe/Si$_{1-x}$Ge$_x$/Si structures) has been established by PL and AFM experiments. PL related to the two-dimensional (2D) buffer layer was always characterized by a NP line and its TO replica at 58 meV in the lower-energy side.

In this section, three main features are discussed: the influence of surface misorientation, the influence of growth temperature (when the substrate is misoriented), and the influence of a two-step process using a self-patterned Si$_{0.7}$Ge$_{0.3}$ template layer to organize the Ge dots [132, 133].

6.1. Influence of substrate misorientation

The results reported in the literature for quantum dots grown on Si(100) substrates show a 2D/3D changeover corresponding to a Ge coverage between 3 and 4 ML [132]. In order to investigate the influence of the substrate orientation on the 2D/3D SK growth mode changeover, we compare PL measurements performed on Si/Ge/Si$_{0.7}$Ge$_{0.3}$/Si(100) and Si/Ge/Si$_{0.7}$Ge$_{0.3}$/Si(118) structures (figure 44). For a Ge coverage of 3 ML (samples B and C in figure 44(a)), we observe the NP and the transverse optical (TO) lines related to the 2D Si$_{0.7}$Ge$_{0.3}$ template layer. The observed energies agree with the Ge content and thickness. If we look at the C sample spectrum, we can observe a new structure. Compared to sample B, although sample C still exhibits the NP/TO pair, its PL spectrum presents a new emission at low energy. This new emission could correspond to the 2D/3D SK growth mode changeover in accordance with the literature results [134]. For a Ge coverage of 7 ML (samples D and F in figure 44(b)), a broad luminescence around 850 meV correlated with the 3D island formation is observed for both orientations. Consequently, we can conclude that the 2D/3D transition starts close to 3 ML for the (100) substrate orientation and later (around 7 ML) for the (118) substrate orientation. Therefore, the substrate orientation strongly influences the nanostructure morphology. AFM characterizations have shown that hut islands are formed on Si(100) surface when wire-shaped islands with reduced lateral size are formed on Si(118) vicinal surfaces. This result is also very promising as regards island size reduction and uniformity.

6.2. Influence of growth temperature

In this section, we want to show that the growth temperature of the Ge monolayers is a determinant parameter for the island growth mechanism. Figure 45 shows the PL signal related
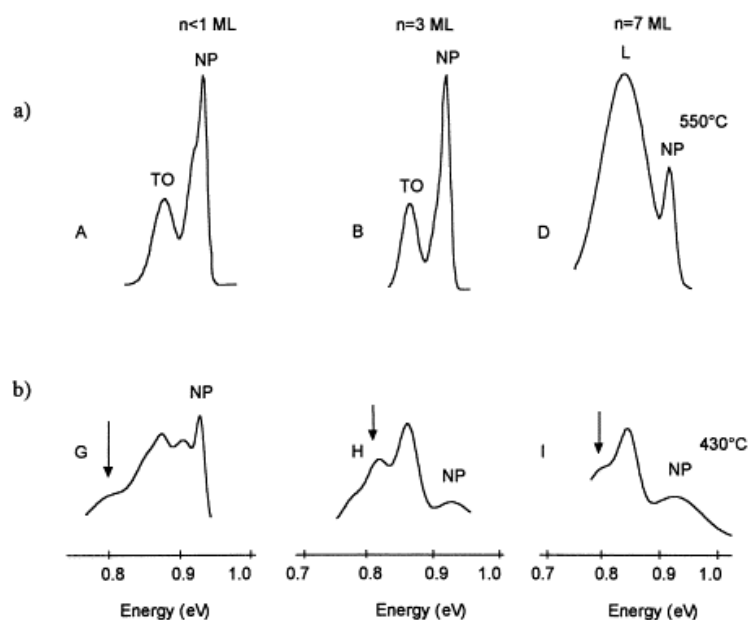
Figure 45. PL spectra of Si/nGe/Si$_{0.7}$Ge$_{0.3}$/Si(118) structures for $n = 1$, 3, and 7 ML obtained at 6 K for two growth temperatures of the Ge coverage: (a) 550 °C, (b) 430 °C.

to samples G, H, and I with a Ge coverage of 1, 3, and 7 ML, deposited at 430 °C. The spectra are quite different compared with figure 45(a), where Ge monolayers were grown at 550 °C. First, at LT, we observe a strong intensity decrease of the luminescence and a new emission which systematically appears at low energy (around 820 meV). In contrast, the intensity of the NP line related to the SiGe wetting layer seems to vanish for Ge coverages of 3 and 7 ML, in comparison with the TO line. Finally, we did not observe the broad band at $n = 7$ ML. We know that, at 430 °C, the growth regime is governed by the hydrogen desorption while at 550 °C the reaction is supply limited. At 430 °C, the SiGe surface is more hydrogen rich than at 550 °C. It is well known that hydrogen can act as a surfactant and may prevent the 2D/3D growth mode changeover. Consequently, at 430 °C, 2D growth is prevailing. This explains the absence of the broad band which indicates that no island was formed. Therefore, the new emission at LT may be correlated with defects due to H adsorption. In conclusion, the growth temperature seems to be a determinant for the island formation.

6.3. *Nature of the recombinations*

In order to study the influence of light on structures grown on Si(118) vicinal surfaces, and to determine the fundamental mechanism of carrier recombination, we have performed PL measurements at 6 K with variable excitation densities. Figure 46 presents the behaviour of sample B ($n = 3$ ML) and sample D ($n = 7$ ML) when the excitation power increases from 0.6 to 20 W cm^{-2}. The peak intensities are normalized to the higher-intensity peak. We observe an important shift (20 meV) of the signal toward the higher energies. This indicates a strong dependence on the excitation power. This behaviour is not conventional in SiGe/Si type-I systems, but it can be explained by a type-II band line-up. In a type-II interface, a two-dimensional electron gas (2DEG) is formed in the conduction band and when the excitation power increases, the 2DEG fills with the photogenerated carriers. This filling induces an energy increase of the transition and hence we observe a blue-shift. Therefore, we have reported in figure 47 the
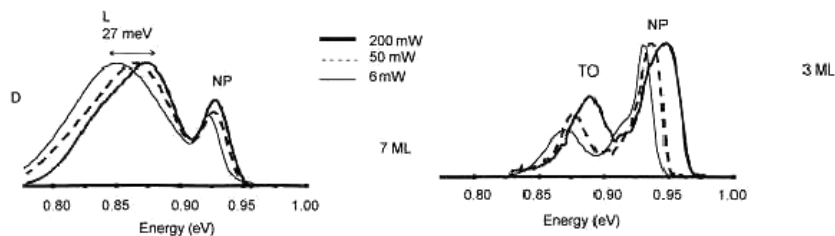
Figure 46. PL spectra of Si/nGe/Si$_{0.7}$Ge$_{0.3}$/Si structures obtained at 6 K for various excitation power densities: $n = 3$ ML (right), $n = 7$ ML (left).
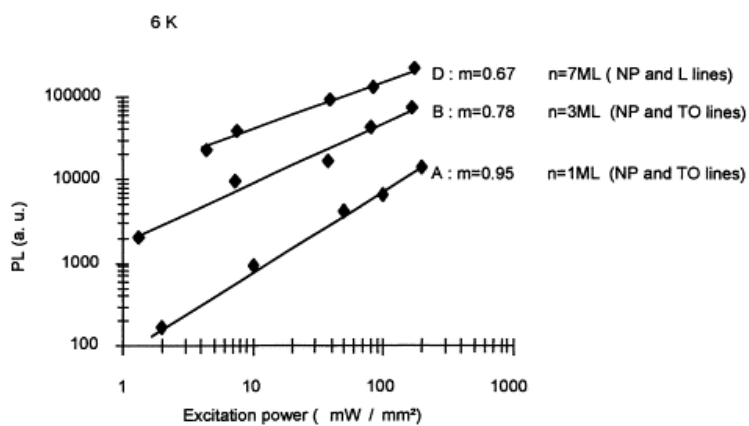

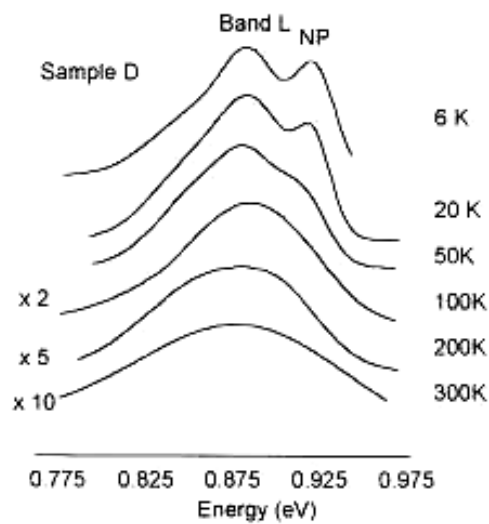**Figure 47.** Excitation power dependence of the PL intensity for Ge coverages of $n = 1$, 3, and 7 ML.

Figure 48. PL spectra of Si/7 ML Ge/SiGe/Si(118) structures obtained at temperatures varying between 6 K and ambient.

coefficient m ($I = P^m$), where I represents the PL intensity and P the power density. For $n = 1$ and 3 ML, m was obtained for the NP/TO pair and for 7 ML m was obtained for the L and NP lines. The coefficient $m < 1$ decreases when the Ge coverage increases. In a type-II interface, the indirect excitons are firstly localized in the interface roughness, then they recombine. But the interface states are limited; hence saturation quickly occurs and $m < 1$. Therefore, when few nanostructures are formed at $n = 7$ ML, they rapidly saturate, particularly for high excitation power. This explains the strong decrease of the coefficient m for the D sample.

6.4. Luminescence temperature

Finally, PL spectra of sample D ($n = 7$ ML) are reported in figure 48 for various temperatures. The PL signal related to the Ge islands persists up to room temperature and the intensity is only reduced by a factor of 10 as compared to LT spectra. In contrast, the 2D luminescence arising from quantum wells disappears around 50 K. This result demonstrates the effect of the spatial confinement of the carriers in the Ge islands up to room temperature. This important property is very promising for optoelectronic device applications.

We have proved that it is possible to engineer PL spectra by making relevant changes in growth conditions. For instance, an increase by a factor of three of the radiative recombination of 2D corrugated systems (consisting of 3 ML of Ge deposited on a $Si_{0.7}Ge_{0.3}$ template layer) when using highly misoriented substrates has been obtained. While the reason for the enhanced intensity is not clear, the influence of the wire-shaped morphology could be invoked. The detrimental effect of decreasing the growth temperature on the optical properties of the samples has been confirmed. Furthermore, some room temperature luminescence experiments have produced results that hold out considerable promise for future applications.

7. Conclusions

In this paper, growth, self-assembly, and properties of $Si_{1-x}Ge_x$ nanostructures have been reviewed. In a general way, kinetic growth parameters and substrate orientation (by way of surface reconstruction, step structure, and step density) were reported to have a peculiar influence on growth modes and relaxation mechanisms.

Both plastic and elastic relaxations were studied as stress-relief processes. As regards the first mechanism, larger experimental critical thicknesses for MD nucleation as compared to the ones derived from standard elastic theories were reported. This was attributed to the influence of kinetics on MD introduction and propagation. In the related framework of SiGe virtual substrate realization, an efficient process using LT pre-deposition of Si was shown. As regards elastic relaxation mechanisms, both chemical and step edge relaxation processes have been addressed. In the first process, the influence of growth conditions (Ge concentration and growth interruption time) on strain-induced Si/Ge interdiffusion has been studied. In the second process, elastic relaxation levels in the layers were found to be associated with the morphology of the layers. In particular, a negligible lateral elastic relaxation in undulating SiGe/Si(001) layers was reported, in contrast to what was expected from various theoretical models. Discrepancies with such models were further observed, when studying SiGe morphological evolution with main growth parameters on (111) and (001) surfaces. For both orientations, experimental kinetic phase diagrams of surface morphologies were extracted. In the (111) case, two growth regimes were observed, according to the SK process. In contrast, in the (001) case, four regimes could be determined and several metastable island morphologies were observed.

The origin of development of SiGe growth instabilities on (001) has also been addressed by comparing the morphological evolution of Si and SiGe layers grown either on nominal

or vicinal (111) and (001) surfaces. Various growth instability regimes (pure kinetic regime, pure and kinetically activated strain-induced regime) were observed. Their dependence on surface orientation/misorientation clearly evidenced the significant role of both kinetics and atomic arrangement of the surface in the origin and evolution of SiGe growth. The potential use of these growth instabilities as templates for growth of assembled Ge nanostructures was finally illustrated. Improvement of SiGe self-organization using an Sb surfactant-mediated Ge growth process was also reported. In this case, very small Ge islands with high density were obtained. This mainly results from the Sb-induced reduction of Ge surface diffusion.

The control of doping of SiGe layers has been studied by addressing Sb and B incorporation/segregation during growth.

Finally, SiGe nanostructure optical properties have been studied by means of PL. Relations between layer growth conditions (and then layer morphologies) and PL spectra have been reported. In particular, in the case of Ge growth on a template substrate, PL intensity was found to be enhanced and to persist up to room temperature.

Acknowledgments

References

[1]   Paul D J 1999 *Adv. Mater.* **11** 191
[2]   Chevrier J, Cruz A, Pinto N, Berbezier I and Derrien J 1994 *J. Physique* I **4** 1309
[3]   Liu W K, Mokler S M, Ohtani N, Roberts C and Joyce B A 1992 *Surf. Sci.* **264** 301
[4]   Gay J M, Stocker P and Réthoré F 1993 *J. Appl. Phys.* **73** 8169
[5]   Bremond G, Serpentini M, Souifi A, Guillot G, Jacquier B, Abdallah M, Berbezier I and Joyce B A 1999 *Microelectron. J.* **30** 35
[6]   Berbezier I, Gallas B and Derrien J 1998 *Surf. Rev. Lett.* **5** 133
[7]   Berbezier I, Gallas B, Ronda A and Derrien J 1998 *Surf. Sci.* **412–3** 415
[8]   Armigliato A, Baldoni R, Corticelli F and Frabboni S 1995 *Microsc. Microanal. Microstruct.* **6** 449
[9]   Matthews J W 1975 *J. Vac. Sci. Technol.* **12** 126
[10]   Hull R and Bean J C 1992 *Crit. Rev. Solid State Mater. Sci.* **17** 507
[11]   Kamat S V and Hirth J P 1990 *J. Appl. Phys.* **67** 6844
[12]   LeGoues F K, Copel M and Tromp R M 1989 *Phys. Rev. Lett.* **63** 1826
[13]   LeGoues F K 1996 *MRS Bull.* **XXI** 38
[14]   Eaglesham D J, Kvam E P, Maher D M, Humphreys C J and Bean J C 1992 *Phil. Mag.* A **59** 2802
[15]   Albrecht M, Christiansen S, Strunk H P, Hansson P O and Bauser E 1993 *Solid State Phenom.* **32–3** 433
[16]   Matthews J W, Jackson D C and Chambers A 1975 *Thin Solid Films* **26** 129
[17]   Van der Merve J H 1963 *J. Appl. Phys.* **34** 117
[18]   Putero M 1999 *PhD Dissertation* University Aix-Marseille III, Marseille
[19]   Pichaud B, Putero M and Burle N 1998 *J. Physique* IV **8** 227
[20]   Gallas B, Hartmann J M, Berbezier I, Abdallah M, Zhang J, Harris J J and Joyce B A 1999 *J. Cryst. Growth* **201–2** 547
[21]   Kvam E P *et al* 1987 *MRS Bull.* **104**
[22]   Fukuda Y, Kohama Y, Seki M and Ochmachi Y 1989 *Japan. J. Appl. Phys.* **28** L19
[23]   Fukuda Y, Kohama Y, Seki M and Ochmachi Y 1988 *Japan. J. Appl. Phys.* **27** 1593
[24]   LeGoues F K, Ott J A, Eberl K and Iyer S S 1992 *Appl. Phys. Lett.* **61** 174
[25]   Beanland R, Aindow M, Joyce T B, Kidd P, Lourenço M and Goodhew P J 1995 *J. Cryst. Growth* **149** 1
[26]   Fernandez J M, Matsumura A, Zhang X M, Lie M H, Hart L and Thornton T J 1995 *J. Mater. Sci.* **6** 330
[27]   Berbezier I, Abdallah M, Ronda A and Bremond G 2000 *Mater. Sci. Eng.* B **69–70** 367
[28]   Ronda A, Abdallah M, Gay J M, Stettner J and Berbezier I 2000 *Appl. Surf. Sci.* **162–3** 576

[29] Pchelyakov O P, Bolkhovityanov Y B, Dvurechenskii A V, Nikiforov A I, Yakimov A I and Voigtländer B 2000 *Thin Solid Films* **367** 75

[30] Mo Y-W, Savage D E, Swartzentruber B S and Lagally M G 1990 *Phys. Rev. Lett.* **65** 1020

[31] Hammar M, LeGoues F K, Tersoff J, Reuter M C and Tromp R M 1996 *Surf. Sci.* **349** 129

[32] Kamins T I, Carr E C, Williams R S and Rosner S J 1997 *J. Appl. Phys.* **81** 211

[33] Liu F, Wu F and Lagally M G 1997 *Chem. Rev.* **97** 1045

[34] Sutter P and Lagally M G 2000 *Phys. Rev. Lett.* **84** 4637

[35] LeGoues F K, Reuter M C, Tersoff J, Hammar M and Tromp R M 1994 *Phys. Rev. Lett.* **73** 300

[36] Gao H 1994 *J. Mech. Phys. Solids* **42** 741

[37] Jesson D E, Chen K M and Pennycook S J 1996 *MRS Bull.* **XXI** 31

[38] Springholz G and Bauer G 1993 *Phys. Rev.* B **48** 10 998

[39] Cullis A G 1996 *MRS Bull.* **XXI** 21

[40] Grilhé J 1993 *Acta Metall. Mater.* **41** 909

[41] Tersoff J and LeGoues F K 1994 *Phys. Rev. Lett.* **72** 3570

[42] Müller P and Kern R 1996 *Appl. Surf. Sci.* **102** 6

[43] Ratsch C, Zangwill A, Smilauer P and Vvedensky D D 1994 *Phys. Rev. Lett.* **72** 3194

[44] Srolovitz D J 1989 *Acta Metall.* **37** 621

[45] Pidduck A, Robbins D, Cullis A, Leong W and Pitt A 1992 *Thin Solid Films* **222** 78

[46] Eaglesham D J, Gossmann H J and Cerullo M 1990 *Mater. Res. Soc. Symp. Proc.* **198** 51

[47] Hull R, Bean J C, Peticolas L J, Bahnck D, Weir B E and Feldman L C 1992 *Appl. Phys. Lett.* **61** 2802

[48] Pchelyakov O P, Markov V A, Nikiforov A I and Sokolov L V 1997 *Thin Solid Films* **306** 299

[49] Deelman P W, Thundat T and Schowalter L J 1996 *Appl. Surf. Sci.* **104–5** 510

[50] Gallas B, Berbezier I, Ronda A and Derrien J 1997 *Thin Solid Films* **294** 22

[51] Volpi F, Portavoce A, Ronda A, Shi Y, Gay J M and Berbezier I 2000 *Thin Solid Films* **380** 46

[52] Wu F, Chen X, Zhang Z Y and Lagally M G 1995 *Phys. Rev. Lett.* **74** 574

[53] Alerhand O L, Vanderbilt D, Meade R D and Joannopoulos J D 1988 *Phys. Rev. Lett.* **61** 1973

[54] Zong L, Hojo A, Matsushita Y, Aiba Y, Hayashi K, Takeda R, Shirai H, Saito H, Matsushita J and Yoshikawa J 1996 *Phys. Rev.* B **54** R2304

[55] Mukherjee S, Pehlke E and Tersoff J 1994 *Phys. Rev.* B **49** 1919

[56] Smilauer P and Vvedensky D D 1995 *Phys. Rev.* B **52** 14 263

[57] Ratsch C, Smilauer P, Vvedensky D D and Zangwill A 1996 *J. Physique* I **6** 575

[58] Siegert M and Plischke M 1994 *Phys. Rev.* E **50** 917

[59] Snyder C W, Mansfield J F and Orr B G 1992 *Phys. Rev.* B **46** 9551

[60] Pierre-Louis P and Misbah C 1996 *Phys. Rev. Lett.* **76** 4761

[61] Rost M, Smilauer P and Krugg J 1996 *Surf. Sci.* **369** 393

[62] Lee N E, Cahill D G and Greene J E 1996 *Phys. Rev.* B **53** 7876

[63] Schelling C, Springholz G and Schäffler F 1999 *Phys. Rev. Lett.* **83** 995

[64] Floro J A, Chason E, Freund L B, Twesten R D, Hwang R Q and Lucadamo G A 1999 *Phys. Rev.* B **59** 1990

[65] Ross F M, Tromp R M and Reuter M C 1999 *Science* **286** 1931

[66] Medeiros-Ribeiro G, Bratkovski A M, Kamins T I, Ohlberg D A A and Williams R S 1998 *Science* **279** 353

[67] Goryll M, Vescan L, Schmidt K, Mesters S, Lüth H and Szot K 1997 *Appl. Phys. Lett.* **71** 410

[68] Jesson D E, Pennycook S J, Baribeau J M and Houghton D C 1993 *Phys. Rev. Lett.* **71** 1744

[69] Asaro R J and Tiller W A 1972 *Metall. Trans.* **3** 1789

[70] Grinfeld M A 1993 *J. Intell. Mater. Syst. Struct.* **4**

[71] Lapena L, Berbezier I, Gallas B and Joyce B 1998 *Thin Solid Films* **336** 124

[72] Berbezier I, Gallas B, Lapena L, Fernandez J, Derrien J and Joyce B 1998 *J. Vac. Sci. Technol.* B **16** 1582

[73] Apetz R, Vescan L, Hartmann A, Dieker C and Lüth H 1995 *Appl. Phys. Lett.* **66** 445

[74] Fukatsu S, Yoshida H, Fujiwara A, Takahashi Y and Shiraki Y 1992 *Appl. Phys. Lett.* **61** 804

[75] Schittenhelm P, Gail M, Brunner J, Nützel J F and Abstreiter G 1995 *Appl. Phys. Lett.* **67** 1292

[76] Noël J P, Rowell N L, Houghton D C and Perovic D D 1990 *Appl. Phys. Lett.* **57** 1037

[77] Kim E S, Usami N and Shiraki Y 1998 *Appl. Phys. Lett.* **72** 1617

[78] Vescan L, Dieker C, Souifi A and Stoica T 1997 *J. Appl. Phys.* **81** 6709

[79] Higgs V, Lightowlers E C, Usami N, Shiraki Y, Mine T and Fukatsu S 1995 *J. Cryst. Growth* **150** 1070

[80] Brunner J, Rupp T S, Gossner H, Ritter R, Eisele I and Abstreiter G 1994 *Appl. Phys. Lett.* **64** 994

[81] Abdallah M, Berbezier I, Dawson P, Serpentini M, Bremond G and Joyce B 1998 *Thin Solid Films* **336** 256

[82] Portavoce A, Ronda A and Berbezier I 2002 *Mater. Sci. Eng.* B **89** 205

[83] Portavoce A, Volpi F, Ronda A, Gas P and Berbezier I 2000 *Thin Solid Films* **380** 164

[84] Metzger R A and Allen F G 1984 *Surf. Sci.* **137** 397

[85] Ladevèze M, Tréglia G, Müller P and Arnaud d'Avitaya F 1998 *Surf. Sci.* **395** 317
[86] Andrieu S and Arnaud d'Avitaya F 1989 *Surf. Sci.* **219** 277
[87] Metzger R A and Allen F G 1984 *J. Appl. Phys.* **55** 931
[88] Falkenberg G, Seehofer L and Johnson R L 1997 *Surf. Sci.* **377–9** 75
[89] Jenkins S J and Srivastava G P 1998 *Surf. Sci.* **398** L308
[90] Portavoce A, Bassani F, Ronda A and Berbezier I 2002 *Surf. Sci.* submitted
[91] Fujita K, Fukatsu S, Usami N, Shiraki Y, Yaguchi H, Ito R and Nakagawa K 1993 *Surf. Sci.* **295** 335
[92] Berbezier I, Gallas B, Fernandez J and Joyce B 1999 *Semicond. Sci. Technol.* **14** 198
[93] Ni W-X, Hansson G V, Cardenas J and Svensson B G 1998 *Thin Solid Films* **321** 131
[94] Ushio J, Nakagawa K, Miyao M and Maruizumi T 1998 *Phys. Rev.* B **58** 3932
[95] Markov I 1994 *Phys. Rev.* B **50** 11 271
[96] Oppo S, Fiorentini V and Scheffler M 1993 *Phys. Rev.* B **71** 2437
[97] Kandel D and Kaxiras E 1995 *Phys. Rev.* B **75** 2742
[98] Jang S M, Liao K and Reif R 1995 *J. Electrochem. Soc.* **142** 3513
[99] Lu M L, Vitkavage J and Meyerson B S 1986 *J. Appl. Phys.* **59** 4032
[100] Lu Q, Bramlett T R, Lee N E, Hasan M A, Karasawa T and Greene J E 1995 *J. Appl. Phys.* **77** 3067
[101] Vick G L and Whittle K M 1969 *J. Electrochem. Soc.* **116** 1142
[102] Meyerson B S, LeGoues F K, Nguyen T N and Harame D L 1987 *Appl. Phys. Lett.* **50** 113
[103] Schubert E F 1993 *Doping in III–V Semiconductors* (Cambridge: Cambridge University Press)
[104] Saitoh N, Akamine T, Aoki K and Kojima Y 1993 *Japan. J. Appl. Phys.* **32** 4404
[105] Gates S M and Koleske D D 1993 *Thin Solid Films* **225** 160
[106] Zhang Z, Kulakov M A, Bullemer B, Eisele I and Zotov A V 1996 *Appl. Phys. Lett.* **69** 494
[107] Larsson M I and Hansson G V 1993 *J. Cryst. Growth* **134** 203
[108] Kim H, Glass G, Park S Y, Spila T, Taylor N, Abelson J R and Greene J E 1996 *Appl. Phys. Lett.* **69** 3869
[109] De Frésart E, Wang K L and Rhee S S 1988 *Appl. Phys. Lett.* **53** 48
[110] Kaxiras E 1993 *Europhys. Lett.* **21** 685
[111] van der Vegt H A, Breeman M, Ferrer S, Etgens V H, Torrelles X, Fajarrdo P and Vlieg E 1995 *Phys. Rev.* B **51** 14 806
[112] Tromp R M and Reuter M C 1992 *Phys. Rev. Lett.* **68** 954
[113] Ohno T 1994 *Phys. Rev. Lett.* **73** 460
[114] Yu B D and Oshiyama A 1994 *Phys. Rev. Lett.* **72** 3190
[115] Fukatsu S, Fujita K, Yaguchi H, Shiraki Y and Ito R 1992 *Surf. Sci.* **267** 79 205
[116] Jorke H 1988 *Surf. Sci.* **193** 569
[117] Ohtani N, Mokler S M, Xie M H, Zhang J and Joyce B A 1993 *Surf. Sci.* **284** 305
[118] Xie M H, Zhang J, Lees A, Fernandez J M and Joyce B A 1996 *Surf. Sci.* **367** 231
[119] Lu X, Jiang Z, Zhu H, Zhang X and Wang X 1996 *Appl. Phys. Lett.* **68** 3278
[120] Wang Y and Hamers R J 1995 *Appl. Phys. Lett.* **66** 2057
[121] Lin H C, Lin H-Y, Chang C-Y, Jung T G, Wang P J, Deng R-C and Lin J 1994 *Am. J. Phys.* **76** 1884
[122] Radamson H H, Joelsson K B, Ni W X, Hultman L and Hansson G V 1995 *J. Cryst. Growth* **157** 80
[123] Chadi D J 1987 *Phys. Rev. Lett.* **59** 1691
[124] Tillack B, Zaumseil P, Morgenstern G, Krüger D and Ritter G 1995 *Appl. Phys. Lett.* **67** 1143
[125] Rodriguez A, Rodriguez T, Sanz-Hervas A, Kling A, Soares J C, da Silva M F, Ballestros C and Gwilliam R M 1997 *J. Mater. Res.* **12** 1698
[126] Sardela M R, Ni J W X, Radpisheh H and Hansson G V 1992 *Thin Solid Films* **222** 42
[127] Glass G, Kim H, Sardela M R, Lu Q, Carlsson J R A, Abelson J R and Greene J E 1997 *Surf. Sci.* **392** L63
[128] Souifi A, Bremond G, Benyattou T, Guillot G, Dutartre D and Berbezier I 1992 *J. Vac. Sci. Technol.* B **10** 2002
[129] Grillot P N, Ringel S A, Michel J and Fitzgerald E A 1996 *J. Appl. Phys.* **80** 2823
[130] Chen H, Cheng W Q, Xie X G, Huang Q and Zhou J M 1997 *Appl. Phys. Lett.* **70** 446
[131] Vescan L, Goryll M, Stoica T, Gartner P, Chretien O, Mateeva E, Dieker C and Hollander B 2000 *Appl. Phys.* A **71** 423
[132] Serpentini M, Souifi A, Abdallah M, Berbezier I and Bremond G 1999 *J. Lumin.* **80** 515–18
[133] Bremond G, Serpentini M, Souifi A, Guillot G and Joyce B 1999 *Microelectron. J.* **30** 357
[134] Sunamura H, Usami N, Shiraki Y and Fukatsu S 1995 *Appl. Phys. Lett.* **66** 3024